

Exploring a lower resolution physics grid in CAM-SE-CSLAM

Adam R. Herrington^{1*}, Peter H. Lauritzen², Kevin A. Reed¹, Steve Goldhaber², Brian E. Eaton²

¹School of Marine and Atmospheric Sciences, Stony Brook University, Stony Brook, New York

²National Center for Atmospheric Research, Boulder, Colorado, USA

Key Points:

- A lower resolution finite-volume physics grid is implemented into CAM-SE-CLAM, containing $\frac{5}{9}$ fewer grid columns than the dynamical core grid.
- Grid imprinting from the spectral-element method is mitigated in regions with steep terrain, using the coarser physics grid.
- The coarser physics grid does not degrade the effective resolution of the model.

*Stony Brook, New York

Corresponding author: Adam R. Herrington, adam.herrington@stonybrook.edu

12 **Abstract**

13 This paper describes the implementation of a coarser resolution physics grid into the Com-
 14 munity Atmosphere Model (CAM), containing $\frac{5}{9}$ fewer grid columns than the dynamics
 15 grid. The dry dynamics is represented by the spectral element dynamical core and tracer
 16 transport is computed using the Conservative Semi-Lagrangian Finite Volume Method
 17 (CAM-SE-CSLAM). Algorithms are presented that map fields between the dynamics and
 18 physics grids while maintaining numerical properties ideal for atmospheric simulations
 19 such as mass conservation and mixing ratio shape and linear-correlation preservation. The
 20 results of experiments using the lower resolution physics grid are compared to the conven-
 21 tional method in which the physics and dynamical grids coincide. The lower resolution
 22 physics grid provides a volume mean state to the physics computed from an equal sam-
 23 pling of the different types of nodal solutions arising in the spectral-element method, and
 24 effectively mitigates grid imprinting in regions with steep topography. The impact of the
 25 coarser resolution physics grid on the resolved scales of motion is analyzed in an aqua-
 26 planet configuration, across a range of dynamical core grid resolutions. The results sug-
 27 gest that the effective resolution of the model is not degraded through the use of a coarser
 28 resolution physics grid. Since the physics makes up about half the computational cost of
 29 the conventional CAM-SE-CSLAM configuration, the coarser physics grid may allow for
 30 significant cost savings with little to no downside.

31 **1 Introduction**

32 Global atmospheric models fundamentally consist of two components. The dynam-
 33 ical core (*dynamics*), which numerically integrate the adiabatic equations of motion and
 34 tracer advection, and the physical parameterizations (*physics*), which compute the effects
 35 of diabatic and subgrid-scale processes (e.g., radiative transfer and moist convection) on
 36 the grid-scale. More out of convenience than anything else, the physics are evaluated on
 37 the dynamics grid, i.e., the physics and dynamics grids coincide. From linear stability and
 38 accuracy analysis of numerical methods, it is a common result that the shortest simulated
 39 wavelengths are not accurately represented by the dynamical core. Additionally, simulated
 40 downscale cascades result in an unrealistic collection of energy and/or enstrophy near the
 41 truncation scale, which may be observed from kinetic energy spectra in model simulations
 42 [Skamarock, 2011]. Some form of dissipation must be incorporated into models to miti-
 43 gate these numerical artifacts near the grid scale [Jablonowski and Williamson, 2011]. The

44 unrealistic nature of the grid-scale led *Lander and Hoskins* [1997] to speculate whether the
 45 physics should be evaluated on a grid that is more reflective of the scales actually resolved
 46 by the dynamical core.

47 Exploring the impact of different physics grid resolutions has so far been limited to
 48 models employing the spectral transform method [*Lander and Hoskins*, 1997; *Williamson*,
 49 1999; *Wedi*, 2014]. *Lander and Hoskins* [1997] argued that passing under-resolved states
 50 to the physics may be especially problematic in spectral transform models, since the physics
 51 are evaluated on a latitude-longitude transform grid, and contains more degrees of free-
 52 dom than the spectral representation to prevent aliasing of quadratic quantities. However,
 53 *Lander and Hoskins* [1997] found that the spectral truncation of the physics tendencies
 54 damps errors that may result from passing an under-resolved state to the physics, although
 55 the extent to which these errors may still be present in the model is difficult to address.

56 Another class of spectral transform models evaluate the quadratic terms using semi-
 57 Lagrangian methods, which are implicitly diffusive, relaxing constraints on the resolution
 58 of the transform grid. *Wedi* [2014] experimented with different transform grid resolutions
 59 and concluded that the standard high resolution quadratic grid actually improves fore-
 60 cast skill over the use of a lower-resolution transform grid. They suggest that increasing
 61 the resolution of the transform grid simulates a kind of sub-grid variability on the spec-
 62 tral state, which is thought to be under-represented in global atmospheric models [*Shutts*,
 63 2005]. This is in principle the purpose of “super-parameterization,” in which a cloud re-
 64 solving model is embedded in each grid cell to approximate sub-grid variability, and im-
 65 proves both diurnal and sub-seasonal variability in the model [*Randall et al.*, 2003].

66 After the physics tendencies are transformed into spectral space, it is possible to
 67 truncate the tendencies at any particular wave number in global spectral transform models.
 68 *Williamson* [1999] conducted a pair of convergence tests using a spectral transform model;
 69 a conventional convergence test and one in which the spectral truncation of the physics
 70 tendencies is held fixed and the resolution of the dynamical core increased. In contrast to
 71 the realistic weather forecasts of *Wedi* [2014], *Williamson* [1999] ran their model to equi-
 72 librium in an idealized climate configuration. When the physics and dynamics resolutions
 73 increase together, as in more typical convergence studies, the strength of the Hadley Cell
 74 increases monotonically with resolution. This sensitivity of Hadley Cell strength to hori-
 75 zontal resolution is a common result of global models at hydrostatic resolutions [see *Her-*

rington and Reed, 2017, and references therein]. But with the truncation wave number of physics tendencies held fixed, the Hadley Cell showed very little sensitivity to dynamical core resolution, resembling the solution for which the dynamics truncation wave number is equal to that of the lower resolution physics. Herrington and Reed [2017] speculated that these results suggest the scales of motion resolved by the dynamical core may be aliased to the lower resolution physics.

Global spectral transform models, while remarkably efficient at small processor counts, do not scale well on massively parallel systems. High-order Galerkin methods are becoming increasingly popular in climate and weather applications due to their high-parallel efficiency, high-processor efficiency, high-order accuracy (for smooth problems), and geometric flexibility facilitating mesh-refinement applications [e.g., Giraldo and Restelli, 2008; Nair *et al.*, 2009; Brdar *et al.*, 2013, and the Energy Exascale Earth System Model; <https://e3sm.org/>]. High resolution climate simulations with NCAR's Community Atmosphere Model [CAM; Neale *et al.*, 2012] are typically performed using a continuous Galerkin dynamical core referred to as CAM-SE [CAM Spectral Elements; Taylor *et al.*, 2008; Dennis *et al.*, 2012; Lauritzen *et al.*, 2018]. CAM-SE may be optionally coupled to a conservative, semi-Lagrangian tracer advection scheme for accelerated multi-tracer transport [CAM-SE-CSLAM; Lauritzen *et al.*, 2017]. Tracer advection then evolves on an entirely separate, finite-volume grid which contains the same degrees of freedom as CAM-SE's quadrature node grid.

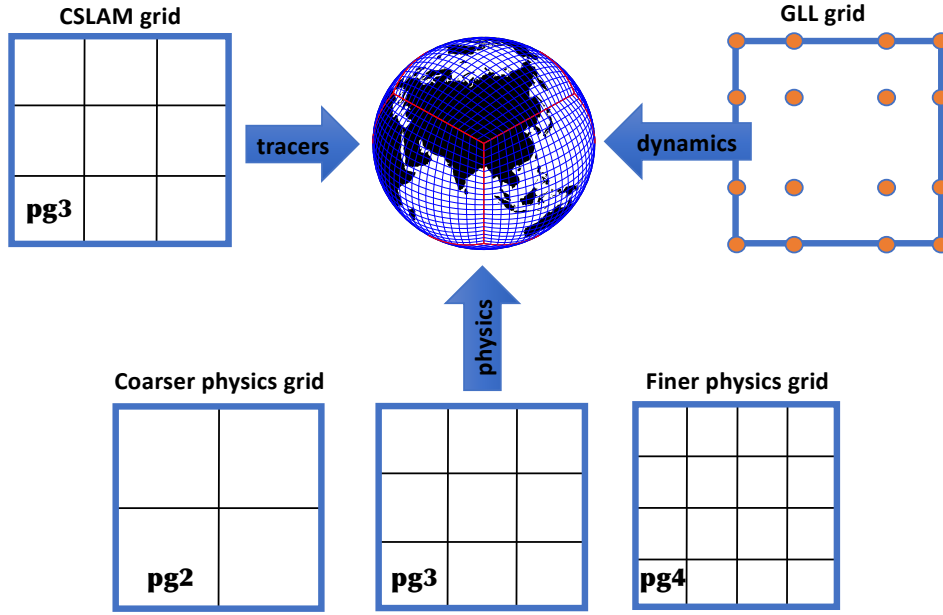
Element-based Galerkin methods are susceptible to grid-imprinting, and may need be considered when contemplating a particular physics grid [Herrington *et al.*, 2018, hereafter referred to as H18]. Grid imprinting manifests at the element boundaries, since the global basis is least smooth (C^0 ; all derivatives are discontinuous) for quadrature nodes lying on the element boundaries, and the gradients (e.g., pressure gradients) are systematically tighter producing local extremes. Through computing the physics tendencies at the nodal points, element boundary extrema is also observed in the physics tendencies.

H18 has shown that through evaluating the physics on the finite-volume tracer advection grid in CAM-SE-CSLAM, element boundary errors are substantially reduced, although still problematic in regions of steep terrain, at low latitudes. Through integrating CAM-SE's basis functions over the control volumes of the finite-volume grid, element boundary extrema is additionally weighted by the C^∞ solutions (i.e., the basis representa-

108 tion is infinitely smooth and all derivatives are continuous) that characterize the interior
 109 of the element, and the state is smoother. Additionally, in defining an area averaged state,
 110 the finite-volume physics grid is made consistent with assumptions inherent to the physics,
 111 and is more appropriate for coupling to other model components (e.g., the land model),
 112 which is typically performed using finite-volume based mapping algorithms.

113 The CAM-SE-CSLAM finite-volume grid is defined through dividing the elements
 114 of CAM-SE's gnomonic cubed-sphere grid with equally spaced, equi-angular coordinate
 115 lines parallel to the equi-angular element boundaries, such that there are 3×3 control
 116 volumes per element (hereafter referred to as $pg3$; see Figure 1). While the physics grid
 117 in H18 is $pg3$, i.e., the physics and dynamics grids have the same degrees of freedom, the
 118 control volumes in $pg3$ encompass a region of the element in which their proximity to the
 119 element boundaries are not equal. Therefore, not every control volume in an element has
 120 the same smoothness properties. This may be avoided through defining a physics grid in
 121 which the elements are instead divided into 2×2 control volumes (hereafter referred to as
 122 $pg2$; see Figure 1). The control volumes of the $pg2$ grid all have the same proximity to
 123 the element boundaries, and should mitigate the element boundary noise that remains in
 124 the $pg3$ grid, and shown in H18.

125 In this study, we test the hypothesis that the coarser, $pg2$ physics grid is effective at
 126 reducing spurious noise at element boundaries, particularly over regions of rough topogra-
 127 phy. In addition, the recent trend towards running models at ever higher resolutions is an
 128 almost prohibitive computational burden. As the physics are responsible for over half of
 129 the computational cost in CAM-SE [Lauritzen *et al.*, 2018], the improvement in computa-
 130 tional performance using a coarser resolution physics grid is potentially significant. How-
 131 ever, any advantages of using a coarser physics grid need be weighed against any potential
 132 reduction in simulation quality, e.g., possible aliasing of the resolved scales of motion by
 133 the coarser grid, as suggested by the results of Williamson [1999]. Section 2 describes the
 134 implementation of the $pg2$ grid into CAM-SE-CSLAM, and the idealized model configu-
 135 rations used throughout this study. Section 3 provides results of model simulations, to test
 136 the implementation of the mapping algorithms and identify any changes in grid imprint-
 137 ing, and in the resolved scales of motion, compared with the $pg3$ configuration. Section 4
 138 provides a discussion of the results and conclusions.



156

Figure 1. An overview of the different grids in CAM-SE-CSLAM.

139

2 Methods

140
141
142
143
144
145
146
147
148
149
150
151
152
153
154
155

Separating dynamics, tracer and physics grids introduces the added complexity of having to map the state from dynamics and tracer grids to the physics grid; and mapping physics tracer increments back to the tracer grid and physics increments needed by the dynamical core to the dynamics grid (see Figure 1). The dynamics grid in the case of CAM-SE-CSLAM refers to the Gauss-Lobatto-Legendre (GLL) quadrature nodes used by the spectral-element method to solve the momentum equations for the momentum vector (u, v), thermodynamics equation for temperature (T), continuity equation for dry air mass ($\frac{1}{g} p$), and continuity equations for water vapor and thermodynamically and inertially active condensates [see, e.g., *Lauritzen et al.*, 2018, for details]. By tracer grid we refer to the $pg3$ grid on which CSLAM performs tracer transport of water vapor, condensates and other tracers. Although water vapor and condensates are being advected by the CSLAM scheme on the $pg3$ grid, these quantities are also needed on the GLL grid for the momentum equations and thermodynamic equation. Transport of water variables is also performed by the spectral-element method on the GLL grid. To avoid decoupling of water species on the CSLAM and GLL grids, the GLL water species are overwritten by the CSLAM values every physics time-step. This is explained in detail in H18.

157 Similarly to the CAM-SE-CSLAM *pg3* configuration, the dynamics state (momentum vector, temperature, dry pressure) must be mapped from the *GLL* grid to the physics
 158 grid. Exactly the same algorithms as used in the *pg3* configuration apply, i.e. momentum
 159 components are interpolated by evaluating the internal Lagrange basis functions (used
 160 in the spectral-element method) at the equi-angular (gnomonic) center of the *pg2* cells
 161 and the Lagrange basis function representations of temperature and pressure are integrated
 162 over the *pg2* control volumes. See H18 for details.
 163

164 As compared to the *pg3* configuration, the extra complication with the *pg2* setup is
 165 that the tracer grid does not coincide with the physics grid, i.e. the tracer state needs to
 166 be mapped from the CSLAM grid (*pg3*) to the physics grid (*pg2*), and tracer increments
 167 computed by physics must be mapped from the physics grid back to the CSLAM grid. In
 168 order to describe the mapping algorithms between the grids some notation needs to be
 169 introduced.

170 The mapping algorithms are applied to each element Ω (with spherical area $\Delta\Omega$) so
 171 without loss of generality consider one element. Let $\Delta A_k^{(pg2)}$ and $\Delta A_\ell^{(pg3)}$ be the spherical
 172 area of the physics grid cell $A_k^{(pg2)}$ and CSLAM control volume $A_\ell^{(pg3)}$, respectively. The
 173 physics grid cells and CSLAM cells, respectively, span the element, Ω , without gaps or
 174 overlaps

$$\cup_{k=1}^{nphys^2} A_k^{(pg2)} = \Omega \text{ and } A_k^{(pg2)} \cap A_\ell^{(pg2)} = \emptyset \quad \forall k \neq \ell, \quad (1)$$

$$\cup_{k=1}^{nc^2} A_k^{(pg3)} = \Omega \text{ and } A_k^{(pg3)} \cap A_\ell^{(pg3)} = \emptyset \quad \forall k \neq \ell, \quad (2)$$

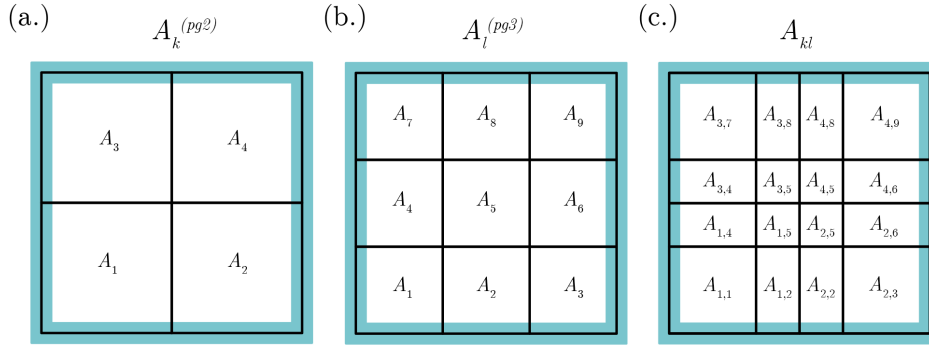
175 where $nc = 3$ is the CSLAM grid resolution parameter and $nphys = 2$ is the physics grid
 176 resolution parameter (following the Fortran code base), although the methods described
 177 here are valid for any arbitrary integer $nphys$ (e.g., $nphys = 4$ is shown in Figure 1). The
 178 overlap areas between the k -th physics grid cell and ℓ th CSLAM cell are denoted

$$A_{k\ell} = A_k^{(pg2)} \cap A_\ell^{(pg3)}, \quad (3)$$

179 (see Figure 2) so that

$$A_k^{(pg2)} = \cup_{\ell=1}^{nc^2} A_{k\ell}. \quad (4)$$

180 This overlap grid is also referred to as the *exchange grid*.



190 **Figure 2.** Indices notation for (a) the $pg2$ grid, (b) the $pg3$ grid and (c) their exchange grid.

181 2.1 Mapping tracers from $A^{(pg3)}$ to $A^{(pg2)}$ (CSLAM to physics grid)

182 The CSLAM and physics grids are both finite-volume grids so existing CSLAM
 183 technology can be used to map the tracer state from CSLAM to physics grid. That is,
 184 compute a high-order shape-preserving reconstruction of mixing ratio m and dry air mass
 185 $\frac{1}{g}\Delta p$ per unit area in each CSLAM control volume and integrate those reconstruction
 186 functions over the overlap areas [Lauritzen *et al.*, 2010; Nair and Lauritzen, 2010]. This
 187 algorithm retains the properties of CSLAM: inherent mass-conservation, consistency (con-
 188 stant mixing ratio is preserved), mixing ratio shape-preservation and linear-correlation
 189 preservation.

191 Denote the known cell averaged values of dry pressure-level thickness and mixing
 192 ratio as $\overline{\Delta p}^{(pg3)}$ and $\overline{m}^{(pg3)}$, respectively. We consider a particular layer and for simplicity
 193 drop the layer subscript. The same procedure is applied to each layer in a column. The
 194 unknowns we would like to compute are the cell-averaged values of the same quantities on
 195 the physics grid; $\overline{\Delta p}^{(pg2)}$ and $\overline{m}^{(pg2)}$, respectively. The dry pressure level thickness inte-
 196 grated over the k 'th physics grid cell is given by

$$\overline{\Delta p}_k^{(pg2)} = \frac{1}{\Delta A_k^{(pg2)}} \sum_{\ell=1}^{nc^2} \langle \delta p \rangle_{k\ell}, \quad (5)$$

197 where $\langle \delta p \rangle_{k\ell}$ is the dry mass in a layer over overlap area $A_{k\ell}$. It is computed by integrat-
 198 ing a high-order (2D polynomial of degree 2) reconstruction of pressure-level thickness in

199 each CSLAM cell over the overlap area $A_{k\ell}$

$$\langle \delta p \rangle_{k\ell} = \int_{A_{k\ell}} \left[\sum_{i+j \leq 2} \mathcal{P}_\ell^{(ij)} x^i y^j \right] dA. \quad (6)$$

200 The reconstruction coefficients $\mathcal{P}_\ell^{(ij)}$ in CSLAM cell ℓ are computed from the cell aver-
 201 age pressure level thicknesses on the CSLAM grid $\overline{\Delta p}^{(pg3)}$ and the numerical integration
 202 over overlap areas is done by line-integrals. The details of that are given in *Lauritzen et al.*
 203 [2010] and not repeated here.

204 The average tracer mass per unit area on the physics grid is given by

$$\overline{m \Delta p}_k^{(pg2)} = \frac{1}{\Delta A_k^{(pg2)}} \sum_{\ell=1}^{nc^2} \langle m \delta p \rangle_{k\ell}, \quad (7)$$

205 where $\langle m \delta p \rangle_{k\ell}$ is the tracer mass over $A_{k\ell}$ resulting from integrating a high-order recon-
 206 struction of Δp and m combined using the approach outlined in Appendix B of *Nair and*
 207 *Lauritzen* [2010] over the overlap area $A_{k\ell}$

$$\langle m \delta p \rangle_{k\ell} = \int_{A_{k\ell}} \left[\overline{\Delta p}_\ell^{(pg3)} \sum_{i+j \leq 2} \mathcal{M}_\ell^{(ij)} x^i y^j + \overline{m}_\ell^{(pg3)} \sum_{i+j \leq 2} \widetilde{\mathcal{P}}_\ell^{(ij)} x^i y^j \right] dA, \quad (8)$$

208 where $\widetilde{\mathcal{P}}_\ell^{(00)} = \mathcal{P}_\ell^{(00)} - \overline{\Delta p}_\ell^{(pg3)}$ and $\widetilde{\mathcal{P}}_\ell^{(ij)} = \mathcal{P}_\ell^{(ij)}$ for $i, j > 0$, and $\mathcal{M}_\ell^{(ij)}$ are the reconstruc-
 209 tion coefficients for the mixing ratio in CSLAM cell $A_\ell^{(pg3)}$. A shape-preserving limiter is
 210 applied to the reconstruction of mixing ratio m [*Barth and Jespersen*, 1989] and not Δp .
 211 This way of combining the reconstruction function for Δp and m in (8) ensures that a con-
 212 stant mixing ratio is preserved (consistency), tracer mass is conserved, linear-correlations
 213 are preserved and tracer shape-preservation is retained. The mixing ratio on the physics
 214 grid is then

$$\overline{m}_k^{(pg2)} = \frac{\overline{(m \Delta p)}_k^{(pg2)}}{\overline{\Delta p}_k^{(pg2)}}, \quad (9)$$

215 where $\overline{\Delta p}_k^{(pg2)}$ is given in (5).

216 Perhaps surprisingly a much more challenging problem is to map tracer increments
 217 (or state) from the physics grid to the CSLAM grid while retaining important properties
 218 such as mass-conservation, consistency, and correlation preservation. Why this mapping
 219 problem is challenging is explained in detail in Section 2.2.1 after having defined impor-
 220 tant properties for mapping physics increments/tendencies.

221 **2.2 Mapping tracer increments from $A^{(pg2)}$ to $A^{(pg3)}$ (physics to CSLAM grid)**

222 The increments from the parameterizations are computed on the physics grid. The
 223 tracer increment in physics grid cell k is denoted $\bar{f}_k^{(pg2)}$ so that the updated mixing ratio
 224 on the physics grid is $\bar{m}_k^{(pg2)} + \bar{f}_k^{(pg2)}$. The problem is how to map $\bar{f}_k^{(pg2)}$ to the CSLAM
 225 control volumes, to obtain $\bar{f}^{(pg3)}$, satisfying the following constraints:

- 226 1. **Local mass-conservation:** At a minimum total physics mass forcing on an element
 227 computed on the physics grid should equal the element physics mass forcing on the
 228 CSLAM grid

$$\bar{f}_k^{(pg2)} \bar{\Delta p}_k^{(pg2)} \Delta A_k^{(pg2)} = \sum_{\ell=1}^{nc^2} \left[\bar{\Delta p}_{\ell}^{(pg3)} \bar{f}_{\ell}^{(pg3)} \Delta A_{k\ell} \right], \quad (10)$$

229 where $\bar{\Delta p}_k^{(pg2)}$ is the pressure level thickness in physics grid cell k and similarly for
 230 $\bar{\Delta p}^{(pg3)}$. We enforce a more local constraint in which only mass-increments over-
 231 lapping with a particular CSLAM cell contributes to the mass-increment in that
 232 CSLAM cell.

- 233 2. **Local shape-preservation in mixing ratio:** The increments mapped to the CSLAM
 234 grid and added to the previous CSLAM state should not produce values smaller
 235 than the updated physics grid mixing ratios, $\bar{m}_k^{(pg2)} + \bar{f}_k^{(pg2)}$, or values smaller than
 236 the existing CSLAM mixing ratios that overlap with physics grid cell A_{ℓ}

$$\bar{m}_{\ell}^{(pg3)} + \bar{f}_{\ell}^{(pg3)} \geq \bar{m}_k^{(min)} = \min \left(\bar{m}_k^{(pg2)} + \bar{f}_k^{(pg2)}, \{ \bar{m}_{k\ell} | \ell = 1, nc^2 \} \right), \quad (11)$$

237 where

$$\bar{m}_{k\ell} = \frac{\langle m \delta p_{k\ell} \rangle}{\langle \delta p_{k\ell} \rangle}. \quad (12)$$

238 The numerator and denominator in (12) are defined in (6) and (8), respectively. In
 239 particular this means that an increment, when mapped to the pg3 grid, should not
 240 drive the state negative (described in detail below as the ‘negativity’ problem).
 241 A similar definition apply for maxima

$$\bar{m}_{\ell}^{(pg3)} + \bar{f}_{\ell}^{(pg3)} \leq \bar{m}_k^{(max)} = \max \left(\bar{m}_k^{(pg2)} + \bar{f}_k^{(pg2)}, \{ \bar{m}_{k\ell} | \ell = 1, nc^2 \} \right), \quad (13)$$

- 242 3. **Linear correlation preservation:** The physics forcing must not disrupt linear tracer
 243 correlation between species on the CSLAM grid [see, e.g., *Lauritzen and Thuburn*,
 244 2012], i.e. if two tracers are linearly correlated and the physics increment preserves
 245 linear correlations on the physics grid then the tracer increment on the CSLAM
 246 grid must not disrupt linear correlations.

247 **4. Consistency:** A non-zero constant mixing ratio increment from physics, $cnst$, on
 248 the physics grid, $\bar{f}_k^{(pg2)} = cnst \forall k$, must result in the same (constant) forcing on the
 249 CSLAM grid, $\bar{f}_\ell^{(pg3)} = \bar{f}_k^{(pg2)} = cnst \forall \ell$.

250 To motivate the algorithm that will simultaneously satisfy 1-4 it is informative to discuss
 251 how ‘standard’ mapping algorithms will violate one or more of the constraints:

252 2.2.1 Why ‘conventional’ conservative remapping will not work

253 It is helpful to analyze in detail why conventional remapping cannot satisfy prop-
 254 erties 1-4 above. Assume that one remaps the mass-increments in exactly the same way
 255 as the mapping of mixing ratio state from the CSLAM grid to the physics grid described
 256 in section 2.1. That is, replace m with f and map from physics grid to the CSLAM grid
 257 instead of the other way around. Denote the mapped mass-increment $\widetilde{f} \Delta p^{(pg3)}$ and due
 258 to the properties of the mapping algorithm the mass-increment is conserved, linear corre-
 259 lation between mass-increments are conserved and shape in mass-increment is preserved.
 260 The problems arise when converting from mass to mixing ratio.

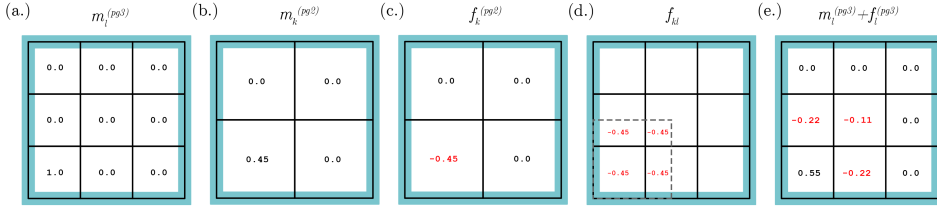
261 *2.2.1.1 Conserve mass but not consistency* If ones uses the known pressure-level
 262 thickness on the CSLAM grid $\bar{\Delta p}_k^{(pg3)}$ to convert from mass-increment to mixing-ratio
 263 increment

$$\bar{m}_k^{(pg3)} = \frac{\widetilde{f} \Delta p_k^{(pg3)}}{\bar{\Delta p}_k^{(pg3)}}, \quad (14)$$

264 a constant mixing ratio increment is not conserved. Basically the constant increment mapped
 265 to the CSLAM grid and converted to mixing ratio increment through (14) will, rather
 266 than being constant, reflect the spurious discrepancy between $\widetilde{\Delta p}_k^{(pg3)}$ and $\bar{\Delta p}_k^{(pg3)}$, where
 267 $\widetilde{\Delta p}_k^{(pg3)}$ is the pressure-level thickness mapped from the pg2 grid to the pg3 grid. That
 268 said, mass will be conserved since the dynamical core state has $\bar{\Delta p}_k^{(pg3)}$ (unless the incre-
 269 ment drives the mixing ratio negative - described in detail below).

270 *2.2.1.2 Consistent but not mass-conserving* Rather than converting to mixing ratio
 271 using $\bar{\Delta p}_k^{(pg3)}$, a constant increment can be preserved by using

$$\bar{m}_k^{(pg3)} = \frac{\widetilde{f} \Delta p_k^{(pg3)}}{\widetilde{\Delta p}_k^{(pg3)}}, \quad (15)$$



275 **Figure 3.** Schematic illustration of the ‘negativity problem’ in a single element. (a.) Initial CSLAM tracer
276 values, (b.) mapped to pg2, (c) produces a tracer increment on pg2, (d.) with negative increments on the ex-
277 change grid overlying CSLAM cells in (a) that were initially zero and (e) driving those mixing ratios negative.

272 instead. But now mass-conservation is lost since, again, $\overline{\Delta p}_k^{(pg2)} \neq \overline{\Delta p}_k^{(pg2)}$. This issue
273 is similar to the mass-wind inconsistency found in specified dynamics applications [e.g.
274 *Jöckel et al., 2001; Lauritzen et al., 2011*].

278 **2.2.1.3 The ‘negativity’ problem and linear correlations** Even if one could derive
279 a reversible map for mapping $\overline{\Delta p}^{(pg2)}$ from the physics grid to the CSLAM grid, there
280 could still be problems if the increment drives the mixing ratios negative (or overshoot-
281 ing occurs) on the CSLAM grid. This can easily happen for tracers, such as cloud liquid
282 amount and cloud ice amount, that are zero in most of the domain and non-zero in local-
283 ized areas/points (where there are clouds). We refer to this as the ‘negativity problem’.
284 This problem is depicted schematically in Figure 3. Consider a single element of CSLAM
285 control volumes, containing only a single cell with mixing ratio 1.0, and 0.0 everywhere
286 else ($\overline{m}_\ell^{(pg3)}$; Figure 3a). The mixing ratios are mapped to the pg2 grid using, for sim-
287 plicity, the piecewise constant method where a constant value inside the pg2 cells is used
288 during the integration over overlap cells ($\overline{m}_k^{(pg2)}$; Figure 3b). Now consider the case in
289 which physics removes all the mass from the physics cell k : $\overline{f}_k^{(pg2)} = -\overline{m}_k^{(pg2)}$ (Figure 3c).
290 The tracer increment is mapped from pg2 to pg3 using the piecewise constant method.
291 Some of the non-zero increments are now in overlap areas where the original CSLAM
292 grid cells have mixing ratio zero ($\overline{f}_{k\ell}$; Figure 3d), and hence, the state is driven negative
293 when adding the overlap increment to the CSLAM state (Figure 3e). This is referred to as
294 the negativity problem although it can also happen for maxima.

The negativity issue could be avoided if one remaps the physics updated state instead of mapping increments/tendencies. In that case a shape-preserving filter will make sure that the state on the CSLAM grid is not negative (and does not overshoot). That said, if physics does not change the state and it is mapped back to the CSLAM grid then spurious tendencies (proportional to the errors introduced by mapping state from the CSLAM grid to the physics grid and back again) are introduced. Hence it is advantageous to map increments/tendencies since any reasonable algorithm will preserve a zero function.

As illustrated above a standard remapping method will NOT simultaneously satisfy 1-4 and hence a new algorithm has been derived.

2.3 New tendency mapping algorithm

The problem is how to map the mass-increment on the physics grid, $\bar{f}^{(pg2)} \Delta A^{(pg2)}$, to the CSLAM cells that overlap with $\Delta A^{(pg2)}$. To maintain shape-preservation, linear correlations and to avoid the negativity problem locally, it is advantageous to define a mass excess function on the exchange grid $\Delta m_{k\ell}^{(excess)}$. It is basically the maximum amount of mixing ratio that can be removed (in the case $\bar{f}^{(pg2)} < 0$) without producing new minima in the exchange grid mixing ratio $m_{k\ell}$

$$\Delta m_{k\ell}^{(excess)} = \bar{m}_{k\ell} - \bar{m}_k^{(min)}, \quad (16)$$

where $\bar{m}_{k\ell}$ is defined in (12). So the maximum amount of mass that we can be removed from the exchange grid cells that span physics grid cell A_k without violating the shape-preservation constraint ((11) and (13)) is

$$\sum_{\ell} \Delta m_{k\ell}^{(excess)} \bar{\Delta p}_{k\ell} \delta A_{k\ell}. \quad (17)$$

If physics is designed not to remove more mass than available in A_k (which should be the case for a carefully designed physics package) then it is guaranteed that

$$\sum_{\ell} \Delta m_{k\ell}^{(excess)} \bar{\Delta p}_{k\ell} \delta A_{k\ell} \geq \bar{f}^{(pg2)} \Delta p_k \Delta A^{(pg2)}. \quad (18)$$

We distribute the physics mass-forcing (assuming $\bar{f}^{(pg2)} < 0$) according to the mass excess in each overlap area by solving this equation for γ_k

$$\Delta A_k^{(pg2)} \bar{\Delta p}_k^{(pg2)} \bar{f}^{(pg2)} = \gamma_k \sum_{\ell} \left[\Delta m_{k\ell}^{(excess)} \bar{\Delta p}_{k\ell} \delta A_{k\ell} \right], \quad (19)$$

and add mass increment (which in this case is negative)

$$\gamma_k \Delta m_{k\ell}^{(excess)} \bar{\Delta p}_{k\ell} \delta A_{k\ell}, \quad (20)$$

319 to the ℓ th CSLAM cell state $\bar{m}^{(pg3)} \bar{\Delta p}_\ell^{(pg3)} \Delta A_\ell^{(pg3)}$. This process is repeated for all physics
 320 cells. Note that this problem is well-posed, i.e. $\gamma_k > 0$, since physics will not remove
 321 more mass than is locally available (18). The way in which the mass-forcing is distributed
 322 to the CSLAM cells using the excess function insures that the negativity problem is avoided.
 323 Mass is conserved by design and shape-preservation is obtained by using the excess func-
 324 tion.

325 If the physics increment is positive (assuming $\bar{f}^{(pg2)} > 0$) we define a ‘lack’ function

$$\Delta m_{k\ell}^{(lack)} = \bar{m}_{k\ell} - \bar{m}^{(max)}, \quad (21)$$

326 and solve

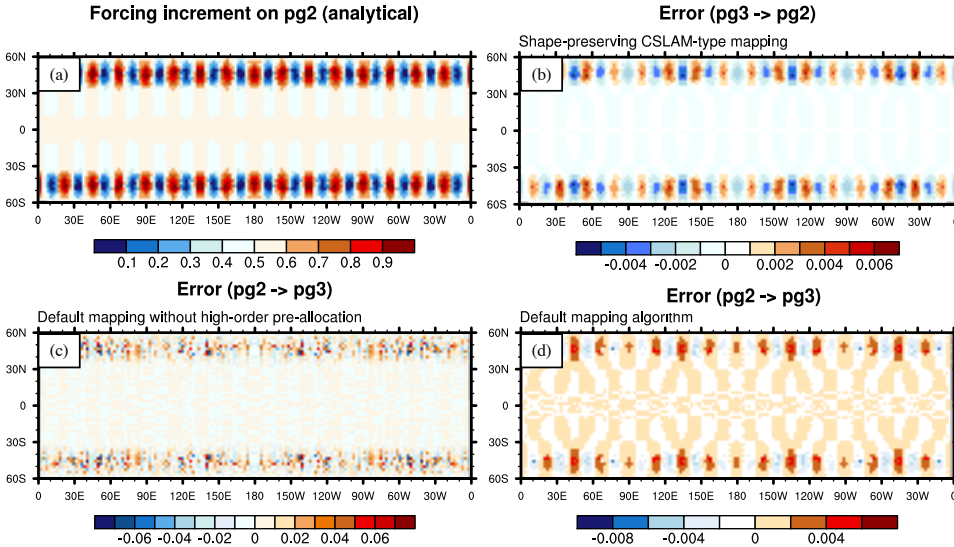
$$\bar{\Delta p}_k^{(pg2)} \bar{f}^{(pg2)} \Delta A_k^{(pg2)} = \gamma_k \sum_\ell \left[\Delta m_{k\ell}^{(lack)} \bar{\Delta p}_{k\ell} \delta A_{k\ell} \right], \quad (22)$$

327 for γ_k and follow the same procedure as for mass excess. Since positive and negative forcing
 328 is treated in exactly the same way, linear correlations are preserved. Note how the def-
 329 inition of the excess/lack function insures linear correlation preservation; for example, if
 330 one would prevent negative values and not do anything about overshoots then linear corre-
 331 lations would not be preserved since the minima and maxima are not treated in the same
 332 way.

333 While the above algorithm satisfies properties 1-4 in section 2.2, it is not a high-
 334 order algorithm in terms of formal accuracy. This is illustrated in Figure ?? (row 3) where
 335 a smooth analytical tendency [approximate spherical harmonic of order 32 and azimuthal
 336 wave number 16; *Jones, 1999*]

$$f^{(pg2)} = \frac{1}{2} + \frac{1}{2} \cos(16\lambda) \sin(2\theta)^{16}, \quad (23)$$

337 where (λ, θ) is latitude-longitude, is mapped from $pg2$ to $pg3$ grid using this algorithm
 338 assuming $m_\ell^{(pg3)} = 0, \forall \ell$. The errors in the mapping are not always aligned with large
 339 gradients in the analytical function as would be expected for a ‘traditional’ interpolation
 340 algorithm. The errors are maximum on the order of 60%. To reduce errors we therefore
 341 perform a higher-order pre-allocation of tendencies that is not mass-conserving but satis-
 342 fies properties 2,3, and 4 in Section 2.2.



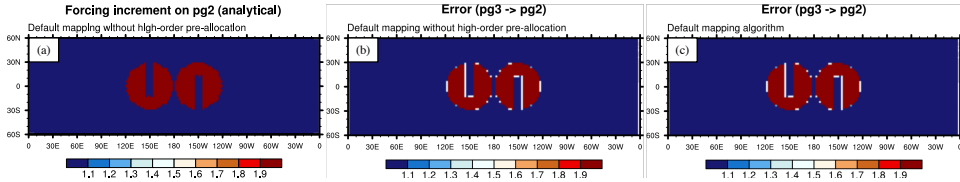
343 **Figure 4.** (a) Smooth analytical function [approximate spherical harmonic of order 32 and azimuthal wave
 344 number 16 referred to as Y_{32}^{16} ; Jones, 1999] plotted using raster contours on the pg2 grid. Remaining plots
 345 show errors (mapped field minus analytical function evaluated at centers of grid cells). In (c) and (d) a Y_{32}^{16}
 346 tracer tendency is mapped from pg2 to pg3 grid using the default mapping algorithm without high-order
 347 pre-allocation algorithm (c) and the default algorithm that uses high-order pre-allocation (d). The Figure
 348 shows that the high-order pre-allocation algorithm used to map tendencies from the pg2 to pg3 grid dras-
 349 tically reduces mapping errors for a smooth function (compare plot (c) and (d)). For comparison the errors
 350 for the high-order CSLAM algorithm used to map state from pg3 to pg2 are shown in plot (b). The errors
 351 for mapping the state from the CSLAM grid to the physics grid are similar in magnitude compared with the
 352 errors arising from mapping tendencies from the physics grid to the CSLAM grid.

359 2.4 High-order (non-conservative) pre-allocation of tracer tendencies

360 A high-order tracer mass increment in overlap area $A_{k\ell}$ can be computed using the
 361 following formula

$$\langle f \delta p \rangle_{k\ell} = \int_{A_{k\ell}} \left[\overline{\Delta p}_\ell^{(pg3)} \sum_{i+j \leq 2} \mathcal{F}_k^{(ij)} x^i y^j + \overline{f}_k^{(pg2)} \sum_{i+j \leq 2} \widetilde{\mathcal{P}}_\ell^{(ij)} x^i y^j \right] dA, \quad (24)$$

362 where $\mathcal{F}_k^{(ij)}$ is the forcing increment reconstruction coefficients in the k th physics grid cell
 363 and $\overline{f}_k^{(pg2)}$ is the average physics increment in the k th physics grid cell. Note that we are
 364 using the known dry pressure reconstruction coefficients on the pg3 grid instead of recon-
 365 structing sub-grid-scale pressure variations from the physics grid cell averaged values. We
 366 can do that since the dry pressure is not modified by physics. This highlights the impor-



353 **Figure 5.** This figure is similar to Figure 4 but for a rough distribution (slotted cylinders). (a) shows the
 354 slotted cylinder distributions on the *pg2* grid plotted using raster contours.
 355 (b) and (c) show the slotted-cylinders after being mapped to the *pg2* grid using the default algorithm without (c) and with (d) the high-
 356 order pre-allocation algorithm. These plots show that the mapping algorithms used to map from *pg2* to the
 357 *pg3* grid are shape-preserving, i.e. no new extrema are created in the mapping process, and they preserve a
 358 constant (the background non-zero field remains constant).

367 tance of a dry-pressure formulation of the dynamical core when separating physics and
 368 dynamics grids [Lauritzen *et al.*, 2018]. If the physics forcing is constant then $\langle f\delta p \rangle_{k\ell}$ ex-
 369 actly equals $\langle \delta p \rangle_{k\ell}$ from (6); in other words, the mapping is designed to be reversible in
 370 dry pressure. The physics increment in terms of mixing ratio change is given by

$$\bar{f}_{k\ell} = \frac{\langle f\delta p \rangle_{k\ell}}{\langle \delta p \rangle_{k\ell}}, \quad (25)$$

371 where the denominator is given by (6).

372 Shape-preservation, as defined by (11) and (13), is enforced by eliminating under
 373 and overshoots on the exchange grid by modifying the forcing increment $\bar{f}_{k\ell}$ so that shape-
 374 preservation is not violated in the overlap areas¹

$$\bar{m}_k^{(min)} \leq \bar{m}_{k\ell} + \tilde{\bar{f}}_{k\ell} \leq \bar{m}_k^{(max)}. \quad (27)$$

375 While this algorithm preserves linear correlations, shape, and is consistent, is it not mass-
 376 conservative. Hence the remaining physics increment not allocated in the algorithm above
 377 is allocated using the new tendency algorithm described in Section 2.3.

¹ In the computation of $\bar{m}_{k\ell}$ there can be small overshoots and undershoots (due to numerical integration errors) compared to the CSLAM cell average values $\bar{m}_\ell^{(pg3)}$ that it overlaps with so we set

$$\bar{m}_k^{(min)} = \min \left(\bar{m}_k^{(min)}, \left\{ \bar{m}_\ell^{(pg)} | \ell = 1, nc^2 \right\} \right) \quad (26)$$

378 Combining the high-order pre-allocation algorithm with the new tendency algo-
 379 rithm (which in this case can also be considered as a mass-fixer that does not disrupt
 380 correlation-preservation, shape and consistency) leads to an order-of-magnitude reduc-
 381 tion in mapping errors for a smooth function (see Figure 4) while fulfilling the mass-
 382 conservation, shape-preservation, linear correlation and consistency constraint. Mass and
 383 linear correlation preservation is illustrated in the baroclinic wave test with terminator
 384 chemistry test in Section 3.1. Shape-preservation and consistency is demonstrated in an
 385 idealized mapping test where a smooth function, see (23), and a slotted-cylinder [see
 386 equation 12 in *Lauritzen et al., 2012*] are mapped to/from the *pg2* and *pg3* grids (Fig-
 387 ure 4 and 5). Since the background value in the mapping of the slotted-cylinder field is
 388 preserved the mapping algorithm is consistent. Since no new over- and undershoots are
 389 produced (particularly obvious in the mapping of the slotted cylinders) the mapping is
 390 shape-preserving. We also note that the mapping errors with the default algorithm (higher-
 391 order pre-allocation with new tendency algorithm) are similar to the errors in mapping the
 392 same field from *pg3* to *pg2* using traditional remapping with CSLAM technology (column
 393 4 in Figure 4).

394 2.5 Model Configurations

395 All simulations in this study are run on the Cheyenne supercomputer hosted at the
 396 NCAR-Wyoming Supercomputer Center [*Computational and Information Systems Lab-*
 397 *oratory, 2017*]. Three model component sets (*compsets*) in the Community Earth Sys-
 398 tem Model, version 2.1 (CESM2.1; <https://doi.org/10.5065/D67H1H0V>) are cho-
 399 sen to carry out the objectives discussed in Section 1. The least complex compset is a
 400 moist baroclinic wave test using a simple, Kessler microphysics scheme [*FKESSLER*
 401 compset; *Lauritzen et al., 2018*]. The baroclinic wave setup is primarily used to evaluate
 402 the new mapping algorithms and their ability to preserve linear-correlations between two
 403 reactive tracers. The role of topography is investigated using a dry Held-Suarez config-
 404 uration [*FHS94* compset; *Held and Suarez, 1994*] modified to include real world topog-
 405 raphy. H18 indicate that this configuration tends to have more grid-noise over steep ter-
 406 rain than in a more complex configuration using CAM, version 6 physics [CAM6; https:////ncar.github.io/CAM/doc/build/html/users_guide/index.html], and is there-
 407 fore a conservative choice for evaluating any change in grid imprinting between *pg3* and
 408 *pg2*.

To understand whether the resolved scales of motion are influenced by a coarser resolution physics grid, a suite of aqua-planet simulations [Neale and Hoskins, 2000; Medeiros *et al.*, 2016] are carried out over a range of spectral-element grid resolutions, using CAM6 physics (*QPC6* compset). The aqua-planet is an ocean covered planet in perpetual equinox, with fixed, zonally-symmetric sea surface temperatures idealized after present day Earth [QOBS in Neale and Hoskins, 2000]. While the dynamics time-step, Δt_{dyn} , varies with resolution according to a CFL criterion, there is no established standard for how the physics time-step, Δt_{phys} , should vary across resolutions. This is further complicated by several studies indicating a high sensitivity of solutions to Δt_{phys} in CAM [Williamson and Olson, 2003; Williamson, 2013; Wan *et al.*, 2015; Herrington and Reed, 2018].

Here, a scaling for Δt_{phys} across resolutions is proposed, based on results of the moist bubble test [Herrington and Reed, 2018] using CAM-SE-CSLAM and detailed in Appendix A. The basis for the scaling is to alleviate truncation errors that arise in the moist bubble test when Δt_{phys} is too large. The scaling is linear in grid-spacing,

$$\Delta t_{phys} = \Delta t_{phys,0} \times \frac{N_{e,0}}{N_e} \text{ s}, \quad (28)$$

where $\Delta t_{phys,0}$ is taken to be the standard 1800s used in CAM-SE-CSLAM at low resolution, $N_{e,0} = 30$ (equivalent to a dynamics grid-spacing of 111.2km). N_e refers to the horizontal resolution of the grid; each of the six panels of the cubed-sphere are divided into $N_e \times N_e$ elements. Throughout the paper, spectral-element grid resolutions are denoted by an ne followed by the quantity N_e , e.g., $ne30$.

CAM-SE-CSLAM uses a hybrid- σ pressure coordinate in the vertical. The *QPC6* (*FKESLLER, FHS94*) compset uses 32 (30) unequally spaced layers disproportionately clustered within the boundary layer and near the tropopause. The same vertical grid is used in all model configurations in this study. The dynamics uses a vertically Lagrangian approach [Lin, 2004], in which the horizontal dynamics evolve within floating Lagrangian layers that are periodically mapped back to a fixed eulerian reference vertical coordinate (sub-cycled twice within in each Δt_{dyn}).

The only other parameter varied across resolutions modulates the strength of explicit numerical dissipation. The spectral element method is not implicitly diffusive, so fourth-order hyper-viscosity operators are applied to the state to suppress numerical artifacts. The

scaling of the hyper-viscosity coefficients, ν , across resolutions is defined as,

$$\nu_T = \nu_{vor} = 0.30 \times \left(\frac{30}{N_e} 1.1 \times 10^5 \right)^3 \frac{m^4}{s}, \quad (29)$$

$$\nu_p = \nu_{div} = 0.751 \times \left(\frac{30}{N_e} 1.1 \times 10^5 \right)^3 \frac{m^4}{s}, \quad (30)$$

where subscripts T , vor , p , div refer to state variables the operators are applied to, temperature, vorticity, pressure and divergence, respectively. The exponent in equation (30) reduces the coefficient by about² an order of magnitude for each doubling of the resolution [as in *Lauritzen et al.*, 2018]. No explicit dissipation of tracers (e.g., water vapor) is required since the semi-Lagrangian numerics in CSLAM are adequately diffusive.

3 Results

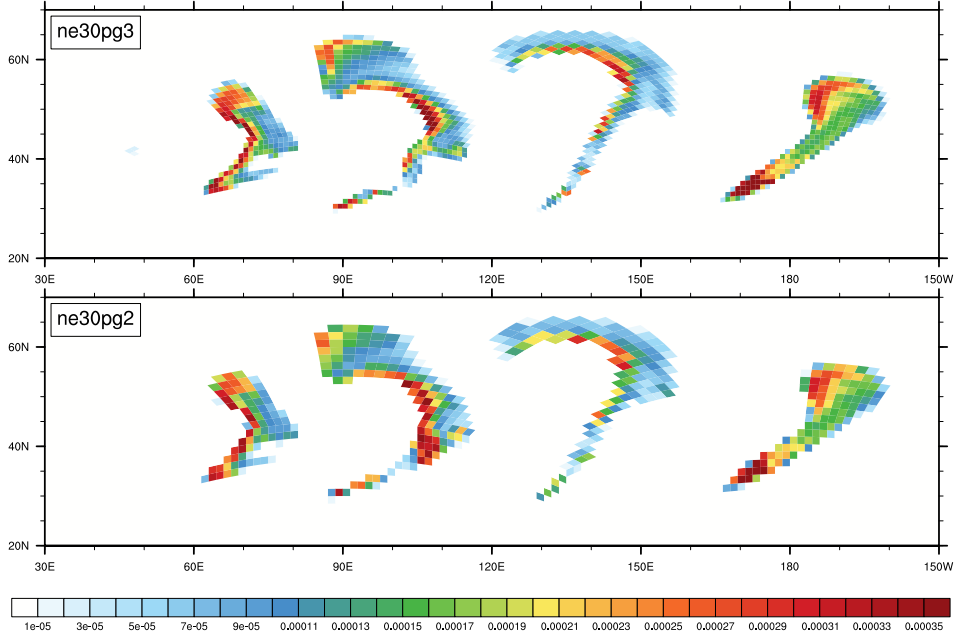
3.1 Mass Conservation and Linear-Correlation Preservation

To illustrate how different the solutions look using the coarser resolution physics grid, Figure 6 shows a snapshot of the cloud liquid field of the moist baroclinic wave test on day 10, in the *ne30pg3* and *ne30pg2* configurations. The cloud liquid fields show in detail clouds forming at wave fronts. As expected, the *pg2* grid looks slightly coarser than *pg3* due to its larger control volumes. Despite this, the details of the wave patterns look reasonably similar to one another.

The model's ability to preserve linear correlations is assessed using the idealized Terminator "Toy" Chemistry test [*Lauritzen et al.*, 2015a, 2017]. The tests consists of two reactive species undergoing photolysis as they are advected over the terminator line. The flow field is provided by the moist baroclinic waves test. The model is initialized with species such that their weighted sum C_{Ly} is a constant, i.e., $C_{Ly} = Cl + 2Cl_2 = 4 \times 10^{-6} \text{ kg kg}^{-1}$. If linear-correlations are preserved, than the column integrated weighted sum of the species, $\langle C_{Ly} \rangle$, is constant.

H18 had shown that in the *ne30pg3* configuration, $\langle C_{Ly} \rangle$ on day 15 of the terminator test is everywhere $4 \times 10^{-6} \text{ kg kg}^{-1}$, to within machine precision. While the *pg3* to *pg2* mapping algorithm in theory preserves linear correlations to machine precision, we found larger than round-off errors in *pg2*, likely due to *if*-logic with machine dependent

² This is approximate. To reduce the coefficients by exactly an order of magnitude for each doubling of the resolution, the exponent should be $\frac{\ln 2}{\ln 10} \approx 3.01029$, which it has been updated to in the most recent version of CESM2.1

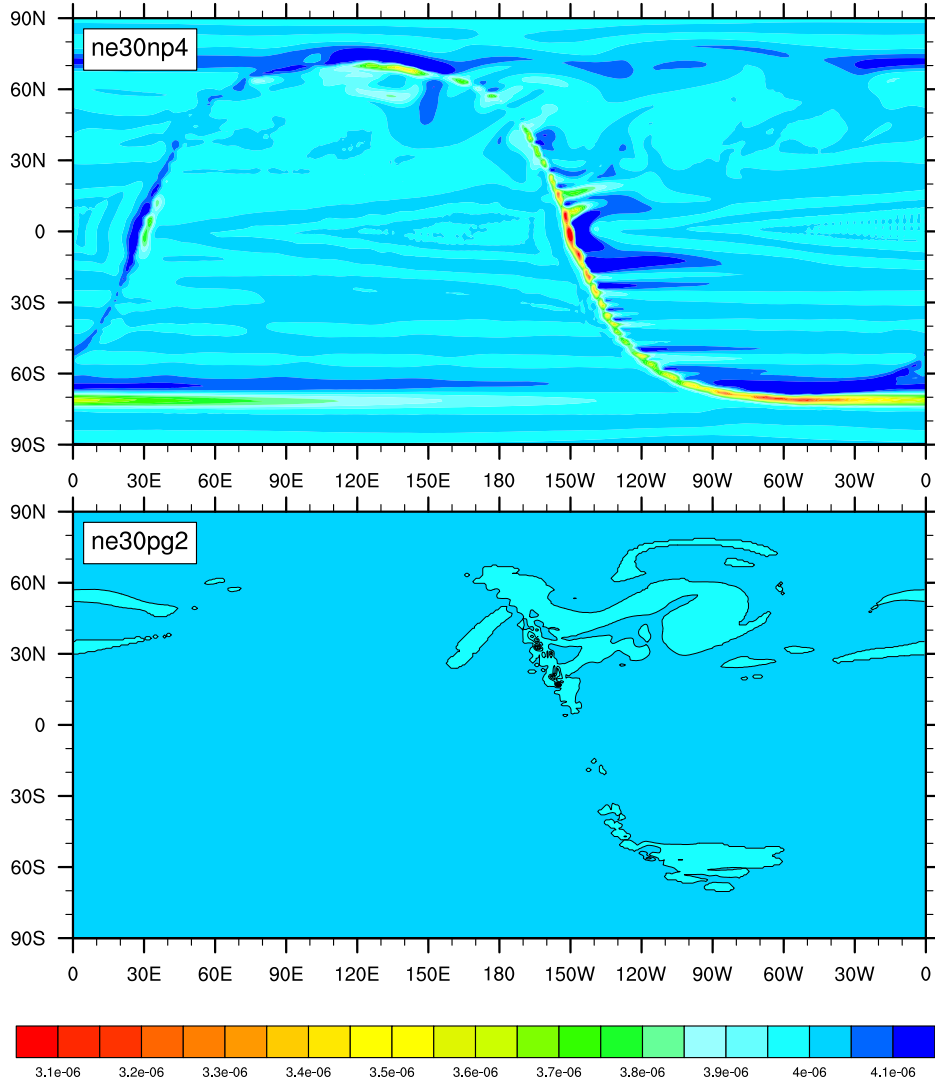


449 **Figure 6.** Snapshot of the cloud liquid field in kg kg^{-1} near the 700hPa level, on day 10 of the moist
 450 baroclinic wave test in the *ne30pg3* and *ne30pg2* configurations, displayed on the upper and lower panels,
 451 respectively. The fields are shown as a raster plot on their respective physics grids.

466 thresholds in the implementation of the algorithm. Figure 7 shows $\langle CLy \rangle$ on day 15 in
 467 the *ne30pg2* configuration, which has a minimum value of $3.99896 \times 10^{-6} \text{ kg kg}^{-1}$, cor-
 468 responding to a maximum relative error of 0.026%³. For comparison, another terminator
 469 test is performed with the equivalent dynamics grid resolution using CAM-SE (*ne30np4*),
 470 in which tracers are advected using the spectral element method. The maximum rela-
 471 tive error in this configuration is 31.6%, three orders of magnitude greater error than the
 472 *ne30pg2* configuration.

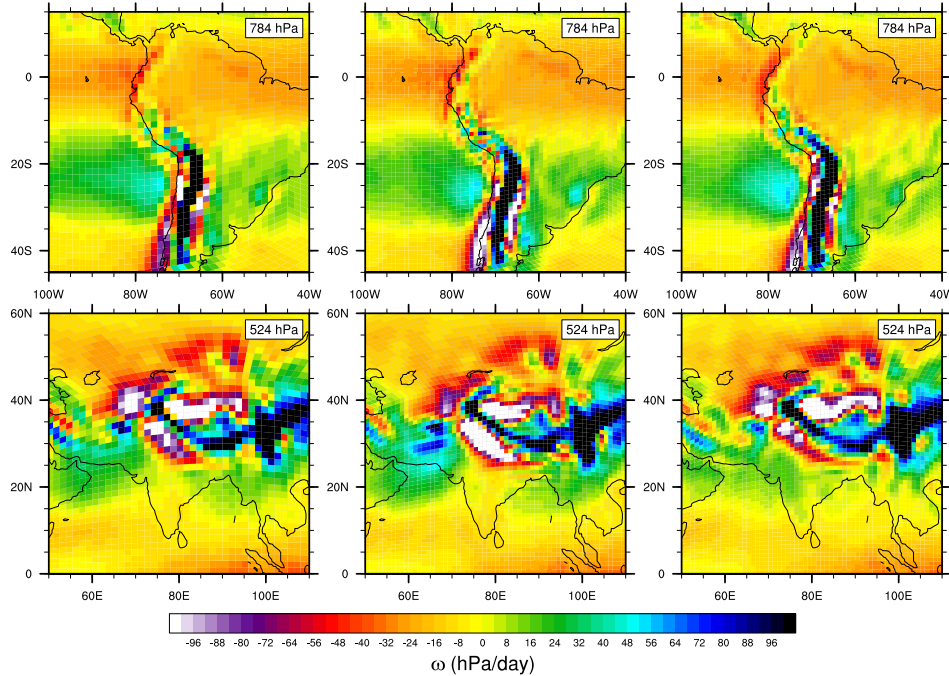
473 Tracer mass conservation is analyzed in a pair of *ne30pg2* and *ne30pg3* aqua-planet
 474 simulations, following the method of *Lauritzen and Williamson* [2019]. Energy and mass
 475 conservation due to a particular model process is assessed by model state I/O before and
 476 after each sub-process in the model. The loss of water vapor mass due to the mapping
 477 algorithms in the *ne30pg2* configuration is estimated as $1.184\text{E}-16 \text{ Pa}$ per time-step, com-
 478 puted as the difference between the the column integrated, global mean climatological wa-

³ The maximum relative error in a *pg2* simulation using a different compiler is 0.016%



459 **Figure 7.** $\langle CL_y \rangle$ in kg kg^{-1} on day 15 of the moist baroclinic wave test in the *ne30np4* and *ne30pg2* con-
 460 figurations, displayed on the upper and lower panels, respectively. The lower panel has a single contour level
 461 of $3.999\text{E-}06 \text{ kg kg}^{-1}$ corresponding to a relative error of 0.025%.

479 ter vapor pressure increment on the physics grid and on the tracer grid. This small error
 480 is effectively zero to within machine precision, and similar to an equivalent calculation in
 481 the *ne30pg3* simulation of $2.171\text{E-}17 \text{ Pa}$ per time-step, which contains no mapping er-
 482 rors since the physics and tracer grids coincide. Negligible mapping error in the *ne30pg2*
 483 configuration is primarily a result of solving equations (19),(22) for γ_k to circumvent the
 484 ‘negativity’ problem. Re-running the *ne30pg2* aqua-planet simulation without this mass
 485 fixer, e.g., through setting $\gamma_k = 1$ and $\Delta m_{k\ell}^{(excess)} = \bar{m}_{k\ell}$ in the mass increment (20), results

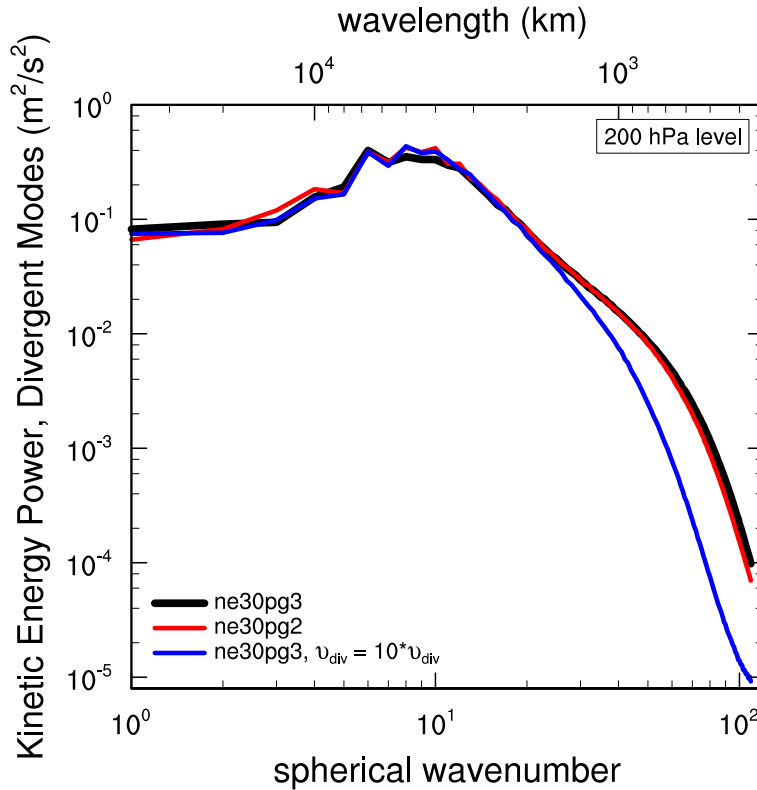


498 **Figure 8.** Mean ω at two model levels in the middle troposphere, in a Held-Suarez configuration outfitted
 499 with real world topography. (Left) *ne30pg2* (Middle) *ne30pg3* and (Right) *ne30pg3* with the divergence
 500 damping coefficient, v_{div} , increased by an order of magnitude. The ω fields are computed from a two-year
 501 simulation. The data are presented on a raster plot in order to identify individual grid cells

486 in a spurious loss of water vapor mass of 2.424E–07 Pa per time-step; the mass fixer is
 487 necessary for conserving tracer mass in *ne30pg2*.

488 3.2 Grid Imprinting

489 Flow over topography can result in significant grid imprinting using the spectral ele-
 490 ment method [Lauritzen *et al.*, 2015b, H18]. Figure 8 shows the results of the Held-Suarez
 491 with topography simulations. The middle panel is the vertical pressure velocity, ω , aver-
 492 aged over two years, over the Andes and Himalayan region at two different levels in the
 493 mid-troposphere, using the *ne30pg3* grid. The fields are displayed as a raster plot on the
 494 physics grid, so that individual extrema, which characterize the flow over the Andes be-
 495 tween about $10^\circ - 20^\circ$ S, may be identified as spurious. Near the foot of the Himalayas,
 496 between about $20^\circ - 30^\circ$ N, there are parallel stripes of extrema aligned with the mountain
 497 front that appear to be spurious $2\Delta x$ oscillations.



512 **Figure 9.** Kinetic energy power spectrum arising from divergent modes in *ne30pg3*, *ne30pg2* and *ne30pg3*
 513 with the divergence damping coefficient, v_{div} , increased by an order of magnitude, in the Held-Suarez with
 514 topography simulations. Spectra computed from five months of six-hourly winds.

502 As discussed in H18, grid imprinting over mountainous terrain tends to occur in re-
 503 gions of weak gravitational stability, causing extrema to extend through the full depth of
 504 the troposphere as resolved updrafts and downdrafts. Thus, grid imprinting over mountains
 505 may be alleviated through increasing the divergence damping in the model. Figure 8 (right
 506 panel) repeats the *ne30pg3* simulation through increasing v_{div} by an order of magnitude.
 507 The spurious noise over the Andes and the Himalayas are damped, and grid point extrema
 508 tend to diffuse into neighboring grid cells. The wavenumber-power spectrum of the ki-
 509 netic energy due to divergent flow (Figure 9) confirms that divergent modes are damped
 510 at higher wavenumbers (greater than 30), by about an order of magnitude relative to the
 511 default *ne30pg3* simulation.

515 The ω field of the *ne30pg2* simulation is provided in Figure 8 (left panel). Grid cell
 516 extrema over the Andes is less prevalent than in the *ne30pg3* simulation, as seen by the

reduction in large magnitude ω (e.g., red grid cells). The spurious oscillations at the foot of the Himalayas appear to have been entirely eliminated. This improvement in grid imprinting is due to the consistent smoothness properties of the control volumes in the *pg2* grid compared with the *pg3* grid discussed in Section 1, and these results are consistent with our hypothesis. The divergent modes are marginally damped relative to *ne30pg3* for wavenumbers greater than about 50, but are an order of magnitude larger than in the enhanced divergence damping *ne30pg3* run (Figure 9). From a scientific and model development perspective, the *pg2* configuration is preferable to the *pg3* configuration, since it eliminates grid imprinting without placing any additional constraints on v_{div} .

3.3 Impact on Resolved Scales of Motion

Tropical regions are very sensitive to horizontal resolution, primarily due to the scale dependence of resolved updrafts and downdrafts at hydrostatic scales [Weisman *et al.*, 1997; Pauluis and Garner, 2006; Jeevanjee, 2017; Herrington and Reed, 2017, 2018]. The vertical velocity of updrafts and downdrafts is related to the horizontal length scales of buoyancy the model is able to support. This can be demonstrated through a scale analysis of the Poisson equation [Jeevanjee and Romps, 2016] valid for hydrostatic scales, showing that the ratio of the scale of ω at two resolutions, due to their respective buoyancies is,

$$\frac{\omega_{\Delta x_1}}{\omega_{\Delta x_2}} = \frac{D_{\Delta x_2}}{D_{\Delta x_1}}, \quad (31)$$

where $D_{\Delta x}$ is a characteristic horizontal buoyancy length scale for grid-spacing Δx (hereafter referred to as the *forcing scale*), and it is presumed that the magnitude of the buoyancy and the vertical scale of the buoyancy is unchanged or compensating across the two resolutions. Equation (31) indicates that the magnitude of the vertical velocity scales like the inverse of the forcing scale, which was verified in a simple moist bubble configuration using CAM-SE and the CAM finite-volume dynamical core [Herrington and Reed, 2018], as well as using CAM-SE-CSLAM as configured in the present study (Appendix A:).

In aqua-planet simulations using CAM-SE, the forcing scale is grid-limited, varying with resolution in the range of five to ten times the grid-spacing [Herrington and Reed, 2018]. Through setting the forcing scale proportional to Δx , equation (31) quantifies the sensitivity of updrafts and downdrafts to horizontal resolution. The forcing scale is analogous to an effective resolution, which is the characteristic length scale below which features are overly damped by numerical dissipation, and largely absent from the solution.

570 **Table 1.** Δx and Δt for the physics and dynamics in the low resolution simulations. Δx is computed as the
 571 average equatorial grid spacing.

Grid name	Δx_{dyn}	Δt_{dyn}	Δx_{phys}	Δt_{phys}
ne20pg3	166.8km	300s	166.8km	1800s
ne30pg2	111.2km	300s	166.8km	1800s
ne30pg3	111.2km	300s	111.2km	1800s

547 The effective resolution may be inferred from kinetic energy spectra as the wavenumber
 548 where the slope of the spectrum becomes steeper than the observationally determined
 549 slope [Skamarock, 2011]. In the CESM2 release of CAM-SE, this criterion occurs near
 550 wavenumber 60 [see Figure 6 in Lauritzen *et al.*, 2018], a length scale of about six times
 551 the grid spacing and overlapping with the estimated forcing scale.

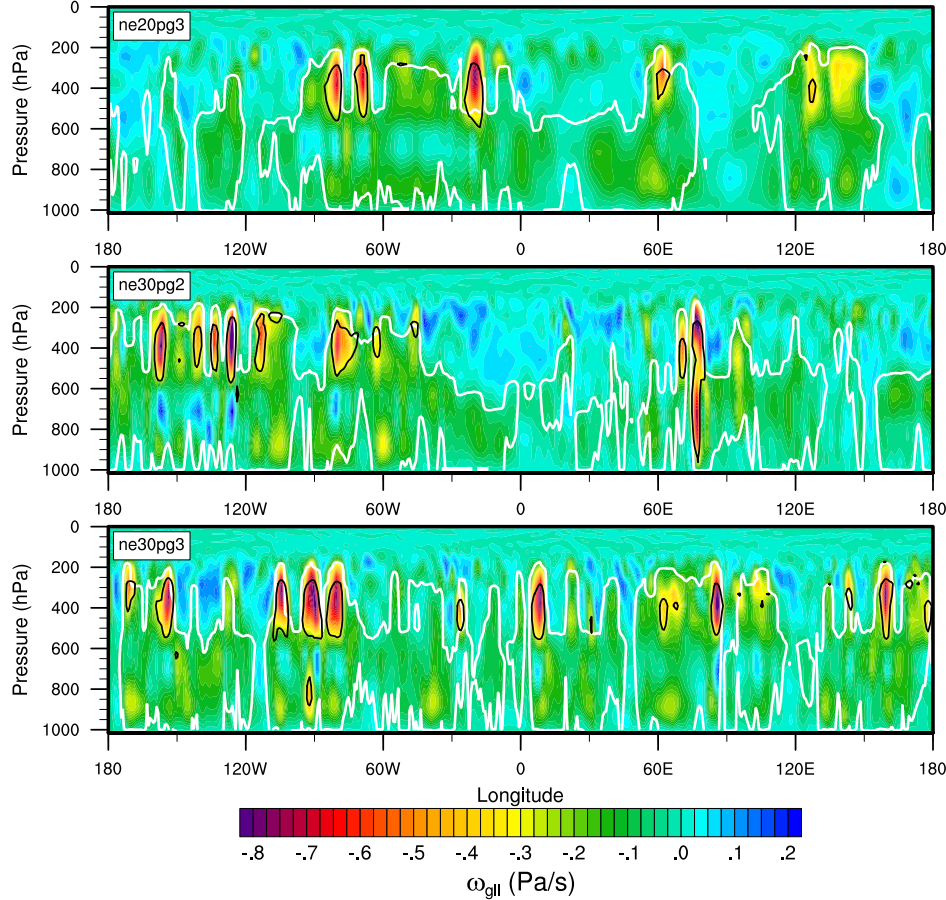
552 When the physics and dynamics grids are of different resolutions, which grid de-
 553 termines the models characteristic forcing scale? The remainder of this section will show
 554 that the dynamics grid spacing largely determines the forcing scale in the pg2 physics grid
 555 configuration. The dynamical core's control over the forcing scale is illustrated at low res-
 556 olution (Section 3.3.1), high resolution (Section 3.3.2) and across a range of resolutions
 557 typical of present day climate models (Section 3.3.3).

558 3.3.1 Low Resolution

559 The question posed above may be addressed through comparing ne30pg2, where
 560 $\Delta x_{phys} = 166.8\text{km}$ (hereafter Δx is expressed as the average equatorial grid spacing), $\frac{3}{2}$
 561 times larger than the dynamics grid spacing, $\Delta x_{dyn} = 111.2\text{km}$, to a simulation where
 562 both are equal to the physics grid spacing, $\Delta x_{dyn} = \Delta x_{phys} = 166.8\text{km}$ (ne20pg3), and
 563 another simulation where both are equal to the dynamics grid spacing, $\Delta x_{dyn} = \Delta x_{phys} =$
 564 111.2km (ne30pg3). The resolvable scales in the ne30pg2 solution are expected to be
 565 bounded by the ne20pg3 and ne30pg3 solutions. Although according to equation (28),
 566 Δt_{phys} for ne20 grids should be different from ne30 grids, here it is set to the ne30 value
 567 (see Table 1) in order to reduce the differences between the three configurations, and
 568 justified because lower resolution runs aren't very sensitive to this range of Δt_{phys} (Fig-
 569 ure A.2).

Figure 10 is a snapshot of the ω field in the Inter-Tropical Convergence Zone (ITCZ) in the pressure-longitude plane, in the three simulations. The ω field is overlaid with the $\pm 15K/day$ contour of the physics temperature tendencies (black), which are primarily due to stratiform cloud formation. Since the component of ω due to buoyancy is determined by the physics temperature tendencies mapped to the GLL grid, the tendencies and ω are shown on the *GLL* grid, $f_T^{(gll)}$ and $\omega^{(gll)}$, respectively. The white contour is intended to outline regions where the deep convection scheme is fairly active, set to the $0.0075kg/m^2/s$ value of the convective mass fluxes (note the convective mass fluxes have not been mapped to the *GLL* grid, and are instead shown on the *pg* grid). The figure indicates that large regions of the ITCZ are comprised of upward ω that balance the warming due to compensating subsidence produced by the deep convection scheme. Much larger magnitude ω are comprised of resolved updrafts driven by the buoyancy of stratiform clouds, and resolved downdrafts due to evaporation of condensates produced by overlying clouds [Herrington and Reed, 2018]. These large buoyancy stratiform clouds tend to form in the middle-to-upper troposphere due to detrainment of moisture from the deep convection scheme [Zhang and McFarlane, 1995].

It is not obvious from the snapshots in Figure 10 whether the length scales of the stratiform clouds, i.e., the models characteristic forcing scale, are any different across the three simulations. Analogous to determining the effective resolution [Skamarock, 2011], the forcing scale may be inferred from the wave-number power spectrum of $f_T^{(gll)}$ as the maximum wavenumber prior to the steep, un-physical decline in power that characterizes the near-grid scale (hereafter $f_T^{(gll)}$ is referred to as the *forcing*). The wave-number power spectrum of the forcing in the middle-to-upper troposphere is shown in Figure 11a. Unlike kinetic energy spectra, the decline in power near the models effective resolution is more gradual, making it difficult to determine a characteristic forcing scale from the spectra. However, it is clear that the slope of the *ne20pg3* spectrum begins to steepen at smaller wavenumbers than in the *ne30pg3* spectra. Additionally, the *ne30pg2* spectra is remarkably similar to the *ne30pg3* spectra, for all wavenumbers. These spectra indicate that the characteristic forcing scale in the *ne30pg2* and *ne30pg3* simulations are similar, and that both are smaller than the *ne20pg3* forcing scale. From equation (31), it is expected that the magnitude of the vertical motion is greater in both the *ne30pg2* and *ne30pg3* simulations.

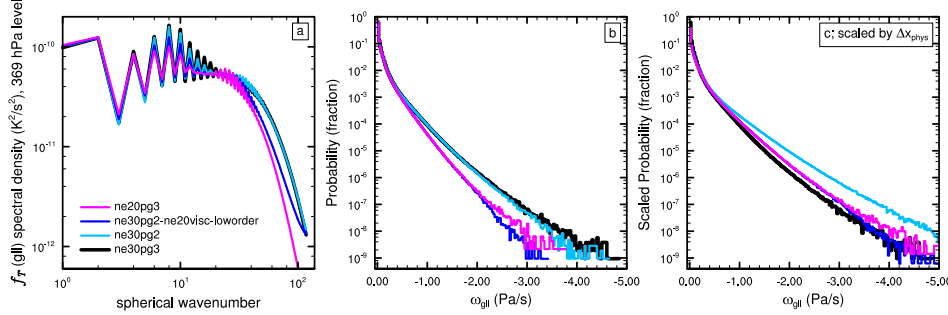


588 **Figure 10.** Snapshots in the longitude-pressure plane of $\omega^{(gll)}$ through the ITCZ region in the *ne20pg3*,
 589 *ne30pg2* and *ne30pg3* configurations, in the upper, middle and lower panels, respectively. Black is the
 590 $\pm 15K/day$ contour of the physics tendencies, and the white contour is the $0.0075kg/m^2/s$ contour of the
 591 parameterized deep convective mass fluxes.

612 The probability density function (PDF) of upward $\omega^{(gll)}$ everywhere in the simula-
 613 tions is shown in Figure 11b. Large magnitude $\omega^{(gll)}$ are more frequent in the *ne30pg2*
 614 run, compared to *ne20pg3*, and the PDF is actually more similar to the *ne30pg3* distribu-
 615 tion, consistent with their similar forcing scales. This may be further illustrated through
 616 scaling the PDF's,

$$P_s(\omega) = \alpha \times P(\omega/\alpha), \quad (32)$$

617 where $P_s(\omega)$ is the scaled PDF of ω and α is the ratio of ω to ω_{target} , the ω associated
 618 with the target grid resolution, Δx_{target} . Making the assumption that the forcing scale is



608 **Figure 11.** (Left) Wavenumber-power spectrum of the temperature tendencies from the moist physics,
 609 near the 369 hPa level, (Middle) probability density distribution and (Right) the scaled probability density
 610 distribution of upward ω everywhere in the model. The scaled distributions are scaled to *ne30pg3* using
 611 Δx_{phys} .

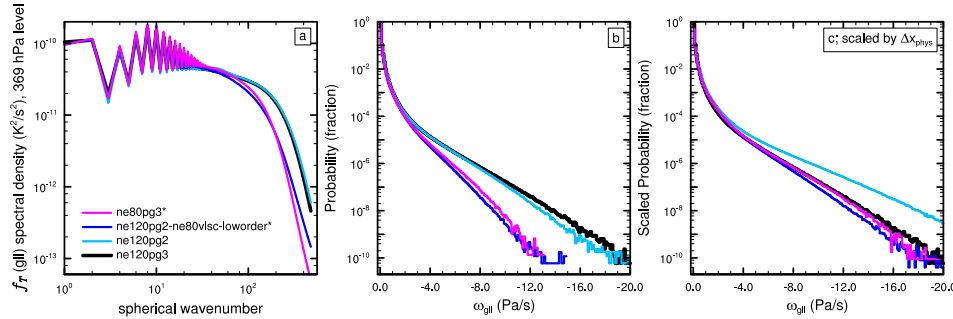
619 linear in Δx , then from equation (31), $\alpha = \Delta x_{target}/\Delta x$. The target resolution is taken
 620 here to be equal to the *ne30pg3* grid resolution.

621 If the forcing scale of *ne30pg2* is in fact determined by Δx_{phys} , then one sets $\Delta x =$
 622 Δx_{phys} in α . This scaled PDF, however, severely overestimates the frequency of upward
 623 ω of the target resolution, *ne30pg3* (Figure 11c). It is clear from the similarity of the
 624 un-scaled PDF's of *ne30pg2* and *ne30pg3* (Figure 11b), and their forcing spectra (Fig-
 625 ure 11a), that the characteristic forcing scale in these two configurations are approximately
 626 the same. It follows that the forcing scales in *ne30pg2* and *ne30pg3* are determined by
 627 their common grid, Δx_{dyn} , rather than Δx_{phys} , which are different. And one can be rea-
 628 sonably confident in the linear framework used to approximate α - the scaled *ne20pg3*
 629 PDF fits the *ne30pg3* distribution quite well. It then follows that the forcing scale of *ne20*
 630 simulations is about $\frac{3}{2}$ times that of *ne30* simulations, the ratio of their grid spacings.

631 There are two reasons the *pg2* forcing scale is determined by the *GLL* grid. The
 632 first being that the hyper-viscosity coefficients are a function of the *GLL* grid resolution
 633 (equation (30)), and the second, that the physics tendencies are mapped to the *pg3* and
 634 *GLL* grids using high-order mapping, which reconstructs scales the *pg2* grid is unable to
 635 support (see Appendix B:). The impact of only using low-order mapping or only using
 636 *ne20* viscosity in a *ne30pg2* simulation results in a forcing spectra that lies in between
 637 the default *ne30pg2* and *ne20pg3* runs (not shown). The combined effect of both fac-
 638 tors on the forcing scale is illustrated through an *ne30pg2* simulation that uses low-order

653 **Table 2.** Δx and Δt for the physics and dynamics in the high resolution simulations. Δx is computed as the
 654 average equatorial grid spacing.

Grid name	Δx_{dyn}	Δt_{dyn}	Δx_{phys}	Δt_{phys}
ne80pg3	41.7km	112.5s	41.7km	675s
ne120pg2	27.8km	75s	41.7km	450s
ne120pg3	27.8km	75s	27.8km	450s



655 **Figure 12.** As in Figure 11, but for the high resolution simulations. Asterisks indicate that $\Delta t_{phys} = 675s$,
 656 which is larger than that used for the default *ne120* runs (see Table 2).

639 mapping, and with hyper-viscosity coefficients set to *ne20* values (*ne30pg2* – *ne20visc* –
 640 *loworder* in Figure 11). The PDF of $\omega^{(gll)}$ and the forcing spectrum more closely resemble
 641 the *ne20pg3* run. In the *ne30pg2-ne20visc-loworder* configuration, the forcing scale
 642 is more accurately determined by Δx_{phys} since the scaled PDF is in fairly good agreement
 643 with the *ne30pg3* simulation (Figure 11c).

644 3.3.2 High Resolution

645 The experiment described in the previous section is repeated here for a *ne120pg2*
 646 aqua-planet simulation, corresponding to an approximate grid spacing of $\Delta x_{dyn} = 27.8km$
 647 and $\Delta x_{phys} = 41.7km$. *ne80pg3* refers to the grid in which the physics and dynamics
 648 are the same resolution as the physics of the *ne120pg2* grid, and *ne120pg3*, the grid in
 649 which the physics and dynamics are equal to the resolution of the dynamics of *ne120pg2*.
 650 At these higher resolutions, the solutions are sensitive to Δt_{phys} (Figure A.2), and so the
 651 *ne80* grid uses a larger time-step than that of the *ne120* grids (Table 2), following equa-
 652 tion (28).

657 Figure 12 is the same as Figure 11, but for the high resolution simulations. While
 658 the *ne80pg3* forcing spectra begins to drop off near wavenumber 100, the *ne120pg2* and
 659 *ne120pg3* drop off closer to wavenumber 200, and their spectra lie on top of one another
 660 (Figure 12a). The PDF's of (upward) $\omega^{(gll)}$ show that the *ne120* distributions lie on top
 661 of one another, and while not a perfect match, both *ne120* runs have substantially more
 662 frequent large magnitude vertical motion than in the *ne80pg3* run (Figure 12b). As in
 663 the low resolution runs, the similarity of the *ne120* forcing spectra and $\omega^{(gll)}$ distribu-
 664 tions indicate that the forcing scale of the *ne120pg2* run is not determined by the physics
 665 grid spacing, but rather the dynamics grid spacing. This is also evident from the over-
 666 prediction of the frequency of large magnitude $\omega^{(gll)}$ compared with the *ne120pg3* run,
 667 through scaling the *ne120pg2* PDF and setting the forcing scale proportional to Δx_{phys} in
 668 equation (32) (Figure 12c).

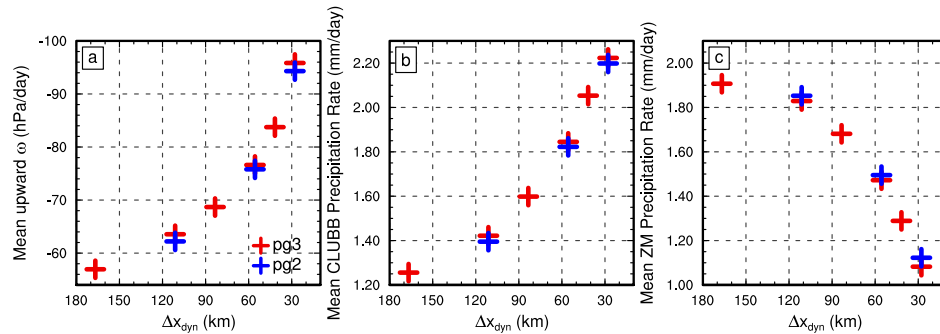
669 In the *ne120pg2* simulation, the dynamics grid determines the forcing scale for
 670 the same two reasons found in the low resolution runs. The high-order mapping of the
 671 physics to the dynamics is important for reconstructing scales not supported on the *pg2*
 672 grid, and scaling the viscosity coefficients by the dynamics grid spacing is also important.
 673 But in order to recreate the *ne80pg3* solution using the *ne120pg2* grid, the physics time-
 674 steps must be the same for these two grids. Combining all three modifications leads to an
 675 *ne120pg2* solution that resembles the *ne80pg3* run (*ne120pg2 – ne80visc – loworder** in
 676 Figure 12). The forcing spectrum and distribution of $\omega^{(gll)}$ match that of the *ne80pg3* run,
 677 and scaling the PDF by Δx_{phys} closely resembles the *ne120pg3* distribution.

678 **3.3.3 Across Resolutions**

679 Three intermediate resolution aqua-planets are run to provide a continuous represen-
 680 tation of the solution spanning from low to high resolution (Table 3). Figure 13 is scat-
 681 ter plot of the climatological global mean state versus Δx_{dyn} for all model configura-
 682 tions listed in Tables 1–3. The fields plotted in the figure, upward ω , and the two components
 683 of precipitation, stratiform precipitation rate (CLUBB) and deep convective precipita-
 684 tion rate (ZM), are all sensitive to resolution. Upward ω and CLUBB precipitation decreases,
 685 and ZM precipitation increases monotonically with Δx_{dyn} . The *pg2* solutions have very
 686 similar values to the *pg3* solutions, although they are slightly offset towards the lower res-
 687 olution side of the plots. The differences between the *pg2* and *pg3* solutions are much
 688 less than the differences between *pg2* and configurations where the physics and dynam-

693 **Table 3.** Δx and Δt for the physics and dynamics in the high resolution simulations. Δx is computed as the
 694 average equatorial grid spacing.

Grid name	Δx_{dyn}	Δt_{dyn}	Δx_{phys}	Δt_{phys}
ne40pg3	83.4km	222.5s	83.4km	1350s
ne60pg2	55.6km	150s	83.4km	900s
ne60pg3	55.6km	150s	55.6km	900s



695 **Figure 13.** Global mean, time-mean (a) upward ω , (b) CLUBB precipitation rate and (c) parameterized
 696 deep convective precipitation rate. All means computed from the final 11 months of one-year simulations, and
 697 upward ω is computed using 6-hourly output.

689 ics grids are both equal to the *pg2* physics grid resolution (e.g., *ne40pg3* compared with
 690 *ne60pg2*). The mean state of the configurations resembles that of the transients discussed
 691 in the previous sections; the coarser *pg2* physics grid does not appear to degrade the re-
 692 solved scales of motion, which are primarily determined by the dynamics grid resolution.

698 4 Conclusions

699 This study documents the implementation of a coarser resolution physics grid into
 700 the Community Atmosphere Model (CAM), with spectral element dynamics (based on
 701 a dry-mass vertical coordinate) and conservative semi-Lagrangian advection of tracers
 702 (CAM-SE-CSLAM). The spectral-element and tracer advection grids are mapped to a
 703 finite-volume physics grid after *Herrington et al.* [2018], but containing $\frac{2}{3}$ fewer degrees
 704 of freedom in each horizontal direction. Mapping from the coarser physics grid to the dy-
 705 namics and tracer grids is performed with high-order reconstructions, and a tendency map-
 706 ping algorithm is developed to ensure shape preservation, consistency, linear-correlation

707 preservation and mass conservation. These numerical properties are verified to a high de-
 708 gree of precision through idealized tests.

709 The coarser resolution physics grid is designed to remove grid imprinting that man-
 710 ifests for non-smooth problems using element-based high-order Galerkin methods. The
 711 lower resolution physics grid provides a volume mean state to the physics that is computed
 712 from an equal sampling of the different types of nodal solutions arising from the spectral-
 713 element method, and it was hypothesized that this method eliminates grid imprinting from
 714 the element boundaries. Using a Held-Suarez configuration modified with real-world to-
 715 topography, it was shown that element boundary noise over steep topography is nearly, if not
 716 entirely eliminated from the coarser physics grid solution, consistent with our hypothesis.

717 Physical parameterizations make up a significant fraction of the total computational
 718 cost of atmosphere models, and the coarser physics grid may be used to reduce this over-
 719 head. The cost savings is due to the factor $\frac{5}{9}$ fewer grid columns in which the physics
 720 need be computed, cutting the physics costs by at least half. In CESM2.0, the CAM6
 721 physics makes up about half the cost of the overall model [Lauritzen *et al.*, 2018], and so
 722 the total cost savings is potentially large, but note that additional mappings between the
 723 tracer advection and physics grids increase the cost of the dynamical core. The authors
 724 sought to understand whether the reduction in computational cost occurs at the expense of
 725 a degraded solution, through aliasing the dynamics to the coarser resolution physics. An
 726 exhaustive number of grids were developed and run in an aqua-planet configuration, and
 727 confirm that the resolved scales of motion are not degraded through the use of a coarser
 728 resolution physics grid. It was found that the resolved scales are primarily determined by
 729 the effective resolution of the dynamical core. This was attributed to two factors; (1), ex-
 730 plicit numerical dissipation by the dynamics blurs the distinction between solutions on
 731 the physics, dynamics or tracer grids, and (2), that high-order mapping of the physics ten-
 732 dencies to the dynamics and tracer grids reconstructs scales that are not supported on the
 733 coarser physics grid.

734 The coarser physics grid in CAM-SE-CSLAM provides significant cost savings with
 735 little to no downside. The coarser physics grid replicates solutions from the conventional
 736 method of evaluating the physics at the same resolution as the dynamical core, mitigates
 737 grid imprinting in the solution and runs efficiently on massively parallel systems. The
 738 coarser physics grid may be leveraged to reduce the computational burden as a component

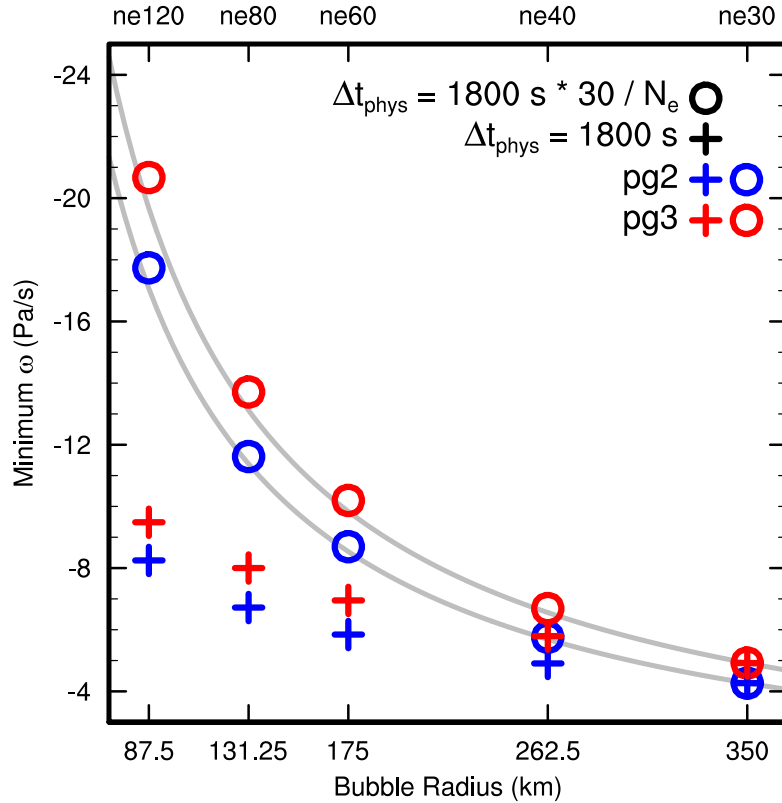
of increasingly expensive Earth System Models, or permit once unattainable throughputs for high-resolution climate simulations. This approach may also be useful in the computationally burdensome “super-parameterization” approach [Randall *et al.*, 2003], in which a cloud resolving model could instead be embedded into the lower resolution physics grid, reducing computational overhead. The coarser physics grid configuration of CAM-SE-CSLAM is well positioned to address the scientific challenges ahead, as a formidable next generation climate model.

746 A: Defining Δt_{phys} across resolutions

747 *Herrington and Reed* [2018] developed a moist bubble test, which indicate that time-
 748 truncation errors are large at high resolution (about 50km or less) using more conventional
 749 values for the physics time-step. The test may be able to provide insight on a reasonable
 750 scaling of Δt_{phys} across resolutions in more complex configurations. In the test a set of
 751 non-rotating simulations are initialized with a warm, super-saturated moist bubble, and
 752 the grid spacing and bubble radius are simultaneously reduced by the same factor in each
 753 run through varying the planetary radius. The test was designed to mimic the reduction in
 754 buoyancy length scales that occur when the model resolution is increased in more complex
 755 configurations [Hack *et al.*, 2006; *Herrington and Reed*, 2018].

756 The moist bubble test is performed with CAM-SE-CSLAM and coupled to the sim-
 757 ple condensation routine of *Kessler* [1969] across five different resolutions (pertaining to
 758 the *ne30*, *ne40*, *ne60*, *ne80*, and *ne120* grids). The results are expressed as the minimum
 759 ω throughout each one day simulation, and shown in Figure A.1. Two sets of simulations
 760 are performed with both *pg3* and *pg2*, one with Δt_{phys} determined by equation (28), and
 761 an equivalent set of simulations with $\Delta t_{phys} = 1800$ s for all resolutions.

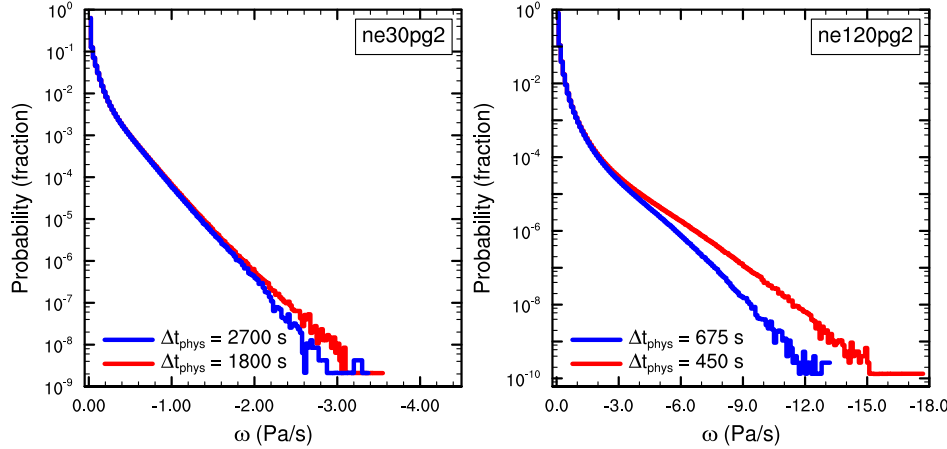
768 With the diameters of the bubbles set proportional to Δx_{dyn} , *Herrington and Reed*
 769 [2018] has shown that ω converges to the scaling of equation (31) in the limit of small
 770 Δt_{phys} , where small Δt_{phys} refers to the CFL limiting time-step used by the dynamics.
 771 Equation (31) is overlain as grey lines in Figure A.1, with *ne30* being the reference reso-
 772 lution. The solutions using Δt_{phys} from equation (28) follow the scaling, whereas fixing
 773 $\Delta t_{phys} = 1800$ s across resolutions damps the solution relative to the analytical solution,
 774 progressively more so at higher resolutions. If Δt_{phys} is too large, the solution has non-
 775 negligible error, which is avoided through scaling Δt_{phys} according to equation (28).



762 **Figure A.1.** Minimum ω from a series of 1-day long moist bubble simulations in which the dynamics grid
 763 spacing (top x-axis) and bubble radius (bottom x-axis) are varied by the same factor. The circles are for experiments
 764 where Δt_{phys} varies according to equation (28), and the crosses for simulations where Δt_{phys} is fixed
 765 at 1800 s. The grey lines are the analytically predicted ω , after equation (31) scaled to the lowest resolution
 766 solutions. The magnitude of ω in the pg3 solutions are systematically larger than the pg2 solutions, which is
 767 primarily a result of the damping effect of integrating the basis functions over a larger control volume.

776 To get a handle on whether the test is useful for understanding more realistic configurations, four aqua-planet simulations are performed using the CAM6 physics package.
 777 A pair of ne30pg2 simulations, one in which Δt_{phys} is set to the appropriate value from
 778 equation (28) (1800s), and another where it is set to the Δt_{phys} corresponding to the ne20
 779 resolution (2700s). Similarly, a pair of ne120pg2 simulations are performed, one with
 780 Δt_{phys} set to the value from equation (28) (450s), and one with Δt_{phys} set to the ne80
 781 value (675s).

786 Figure A.2 shows the PDFs of upward ω computed from a year of six-hourly data
 787 in the simulations. At lower resolution, Δt_{phys} has only a very small effect on the solu-



783 **Figure A.2.** Probability density distribution of upward ω everywhere in the model in the aqua-planets using
 784 the *ne30pg2* grid (Left) and the *ne120pg2* grid (Right). Figure computed for one year of 6-hourly data. The
 785 different colors indicate the physics time-steps used in the runs.

788 tion, near the tale-end of the distributions. At high-resolution, values of ω less than about
 789 -3Pa/s are more frequent in the small Δt_{phys} run, with the discrepancy growing more for
 790 larger magnitudes of ω . The progressively larger errors with increasing resolution also
 791 manifests in the moist bubble tests, indicating that truncation errors arising from large
 792 Δt_{phys} do exist in more complex configurations.

793 **B: The impact of high-order mapping to the dynamics grids**

794 Figure B.1a shows a close-up of the wavenumber power spectrum of the forcing on
 795 the *pg* grid (dotted), where it is computed, and on the *GLL* grid (solid), where it is has
 796 been mapped. In *ne30pg3*, the magnitudes are similar on both grids, except the mapping
 797 tends to damp the high wavenumbers of the forcing on the *GLL* grid (greater than 60),
 798 but these scales are primarily below the effective resolution of the model and should not
 799 effect the solution. For *ne30pg2*, the magnitude of the forcing is actually greater after
 800 mapping to the *GLL* grid, and more similar to the forcing in the *ne30pg3* simulations.
 801 The high-order mapping can therefore replicate the scales of the physics tendencies that
 802 occur in the *pg3* simulation, even though the physics are evaluated on a coarser *pg2* grid.

807 The importance of the high-order mapping can be shown with an additional *ne30pg2*
 808 simulation, using low-order mapping (*ne30pg2 – loworder* in Figure B.1). Specifically,

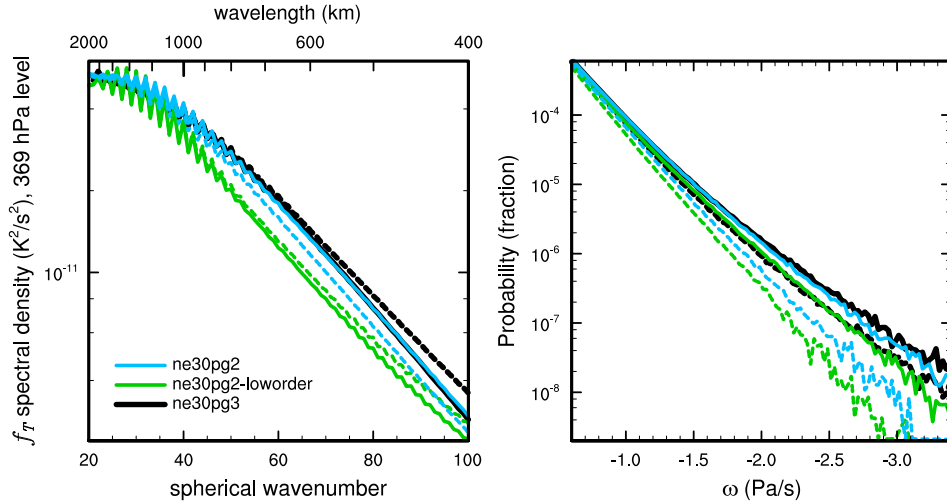


Figure B.1. (Left) Wavenumber-power spectrum of the temperature tendencies from the moist physics, at the 369 hPa level, and (right) probability density distribution of upward ω , everywhere in the model, for three year-long aqua-planet simulations. Solid lines refer to values of on the *GLL* grids, and dashed lines, the fields on the *pg* grids. See text for details regarding the three simulations.

low-order mapping refers to piecewise constant mapping between the *pg2* and *CSLAM* grids, and bi-linear mapping from *pg2* to the *GLL* grid. The forcing spectrum is now similar on both the *pg2* and *GLL* grids, although the low-order mapping tends to damp the forcing on the *GLL* grid for wavenumbers greater than about 60, scales smaller than the models effective resolution (Figure B.1a). A close up of the PDF of $\omega^{(gll)}$ is provided in Figure B.1b (solid lines). As expected, the frequency of large magnitude $\omega^{(gll)}$ in the low-order run is less compared to the default *ne30pg2* simulation.

The dotted lines in Figure B.1b show the PDF of ω on the *pg* grids. The frequency of large magnitude ω is reduced on the *pg* grids, compared to the state on the *GLL* grids. This is primarily due to the smoothing effect of integrating the nodal point values over control volumes (H18). The larger ω values are even less frequent on the *pg2* grid due to integrating over control volumes $\frac{9}{4}$ times greater than the *pg3* control volumes.

Acknowledgments

The CESM project is supported primarily by the National Science Foundation (NSF). This material is based upon work supported by the National Center for Atmospheric Research (NCAR), which is a major facility sponsored by NSF under Cooperative Agreement No.

825 1852977. Computing and data storage resources, including the Cheyenne supercomputer
 826 (doi:10.5065/D6RX99HX), were provided by the Computational and Information Systems
 827 Laboratory (CISL) at NCAR. Herrington, Reed, and Lauritzen are indebted to the NCAR
 828 Advanced Study Program graduate visitor program for funding Herrington's 12-month
 829 visit. Reed was partially supported by U.S. Department of Energy Office of Science grant
 830 DE-SC0019459. Goldhaber was partially supported by the U.S. Department of Energy
 831 Office of Biological and Environmental Research, Work Package 12-015334 "Multiscale
 832 Methods for Accurate, Efficient, and Scale-Aware Models of the Earth System". Model
 833 output used in this study is publicly available from <https://github.com/adamrher/2017-physres/tree/master/data>.

835 References

- 836 Barth, T., and D. Jespersen (1989), The design and application of upwind schemes on un-
 837 structured meshes., *Proc. AIAA 27th Aerospace Sciences Meeting, Reno*.
- 838 Brdar, S., M. Baldauf, A. Dedner, and R. Klöfkorn (2013), Comparison of dynamical
 839 cores for nwp models: comparison of cosmo and dune, *Theoretical and Computational
 840 Fluid Dynamics*, 27(3-4), 453–472, doi:10.1007/s00162-012-0264-z.
- 841 Computational and Information Systems Laboratory (2017), Cheyenne: HPE/SGI ICE XA
 842 System (AMP Model Developments), doi:10.5065/D6RX99HX.
- 843 Dennis, J. M., J. Edwards, K. J. Evans, O. Guba, P. H. Lauritzen, A. A. Mirin, A. St-Cyr,
 844 M. A. Taylor, and P. H. Worley (2012), CAM-SE: A scalable spectral element dynami-
 845 cal core for the Community Atmosphere Model, *Int. J. High. Perform. C.*, 26(1), 74–89,
 846 doi:10.1177/1094342011428142.
- 847 Giraldo, F., and M. Restelli (2008), A study of spectral element and discontinuous
 848 galerkin methods for the Navier-Stokes equations in nonhydrostatic mesoscale atmo-
 849 spheric modeling: Equation sets and test cases, *J. Comput. Phys.*, 227(8), 3849 – 3877,
 850 doi:<http://dx.doi.org/10.1016/j.jcp.2007.12.009>.
- 851 Hack, J., M. Caron, G. Danabasoglu, K. W. Oleson, C. Bitz, and J. Truesdale (2006),
 852 CCSM–cam3 climate simulation sensitivity to changes in horizontal resolution, *J. Cli-
 853 mate*, 19(1), 2269–2289, doi:10.1175/JCLI3764.1.
- 854 Held, I. M., and M. J. Suarez (1994), A proposal for the intercomparison of the dynamical
 855 cores of atmospheric general circulation models, *Bull. Am. Meteorol. Soc.*, 73, 1825–
 856 1830.

- 857 Herrington, A., and K. Reed (2018), An idealized test of the response of the commu-
858 nity atmosphere model to near-grid-scale forcing across hydrostatic resolutions, *J. Adv.*
859 *Model. Earth Syst.*, 10(2), 560–575.
- 860 Herrington, A., P. Lauritzen, M. A. Taylor, S. Goldhaber, B. E. Eaton, J. Bacmeister,
861 K. Reed, and P. Ullrich (2018), Physics-dynamics coupling with element-based high-
862 order galerkin methods: quasi equal-area physics grid, *Mon. Wea. Rev.*, 47, 69–84, doi:
863 10.1175/MWR-D-18-0136.1.
- 864 Herrington, A. R., and K. A. Reed (2017), An explanation for the sensitivity of the mean
865 state of the community atmosphere model to horizontal resolution on aquaplanets, *J.*
866 *Climate*, 30(13), 4781–4797, doi:10.1175/jcli-d-16-0069.1.
- 867 Jablonowski, C., and D. L. Williamson (2011), The pros and cons of diffusion, filters and
868 fixers in atmospheric general circulation models., in: P.H. Lauritzen, R.D. Nair, C.
869 Jablonowski, M. Taylor (Eds.), Numerical techniques for global atmospheric models,
870 *Lecture Notes in Computational Science and Engineering*, Springer, 80.
- 871 Jeevanjee, N. (2017), Vertical velocity in the gray zone, *Journal of Advances in Modeling*
872 *Earth Systems*, 9(6), 2304–2316, doi:10.1002/2017MS001059.
- 873 Jeevanjee, N., and D. M. Romps (2016), Effective buoyancy at the surface and aloft,
874 *Quart. J. Roy. Meteor. Soc.*, 142(695), 811–820.
- 875 Jöckel, P., R. von Kuhlmann, M. G. Lawrence, B. Steil, C. Brenninkmeijer, P. J. Crutzen,
876 P. J. Rasch, and B. Eaton (2001), On a fundamental problem in implementing flux-form
877 advection schemes for tracer transport in 3-dimensional general circulation and chem-
878 istry transport models., *Q.J.R. Meteorol. Soc.*, 127(573), 1035–1052.
- 879 Jones, P. W. (1999), First- and second-order conservative remapping schemes for grids in
880 spherical coordinates, *Mon. Wea. Rev.*, 127, 2204–2210.
- 881 Kessler, E. (1969), On the distribution and continuity of water substance in atmospheric
882 circulations, *Meteorol. Monogr.*, 10(32), 88.
- 883 Lander, J., and B. Hoskins (1997), Believable scales and parameterizations in a spectral
884 transform model, *Mon. Wea. Rev.*, 125, 292–303., doi:10.1175/1520-0493.
- 885 Lauritzen, P., and J. Thuburn (2012), Evaluating advection/transport schemes using inter-
886 related tracers, scatter plots and numerical mixing diagnostics, *Quart. J. Roy. Met. Soc.*,
887 138(665), 906–918, doi:10.1002/qj.986.
- 888 Lauritzen, P. H., and D. L. Williamson (2019), A total energy error analysis of dynamical
889 cores and physics-dynamics coupling in the community atmosphere model (cam), *J.*

- 890 *Adv. Model. Earth Syst.*, doi:10.1029/2018MS001549.
- 891 Lauritzen, P. H., R. D. Nair, and P. A. Ullrich (2010), A conservative semi-Lagrangian
892 multi-tracer transport scheme (CSLAM) on the cubed-sphere grid, *J. Comput. Phys.*,
893 229, 1401–1424, doi:10.1016/j.jcp.2009.10.036.
- 894 Lauritzen, P. H., P. A. Ullrich, and R. D. Nair (2011), Atmospheric transport schemes:
895 desirable properties and a semi-Lagrangian view on finite-volume discretizations, in:
896 P.H. Lauritzen, R.D. Nair, C. Jablonowski, M. Taylor (Eds.), Numerical techniques for
897 global atmospheric models, *Lecture Notes in Computational Science and Engineering*,
898 Springer, 2011, 80, doi:10.1007/978-3-642-11640-7_8.
- 899 Lauritzen, P. H., W. C. Skamarock, M. J. Prather, and M. A. Taylor (2012), A standard
900 test case suite for 2d linear transport on the sphere, *Geo. Geosci. Model Dev.*, 5, 887–
901 901.
- 902 Lauritzen, P. H., A. J. Conley, J.-F. Lamarque, F. Vitt, and M. A. Taylor (2015a), The ter-
903 minator "toy" chemistry test: a simple tool to assess errors in transport schemes, *Geo-*
904 *scientific Model Development*, 8(5), 1299–1313, doi:10.5194/gmd-8-1299-2015.
- 905 Lauritzen, P. H., J. T. Bacmeister, P. F. Callaghan, and M. A. Taylor (2015b), Ncar global
906 model topography generation software for unstructured grids, *Geoscientific Model Devel-*
907 *opment Discussions*, 8(6), 4623–4651, doi:10.5194/gmdd-8-4623-2015.
- 908 Lauritzen, P. H., M. A. Taylor, J. Overfelt, P. A. Ullrich, R. D. Nair, S. Goldhaber, and
909 R. Kelly (2017), CAM-SE-CSLAM: Consistent coupling of a conservative semi-
910 lagrangian finite-volume method with spectral element dynamics, *Mon. Wea. Rev.*,
911 145(3), 833–855, doi:10.1175/MWR-D-16-0258.1.
- 912 Lauritzen, P. H., R. Nair, A. Herrington, P. Callaghan, S. Goldhaber, J. Dennis, J. T.
913 Bacmeister, B. Eaton, C. Zarzycki, M. A. Taylor, A. Gettelman, R. Neale, B. Dob-
914 bins, K. Reed, and T. Dubos (2018), NCAR CESM2.0 release of CAM-SE: A refor-
915 mulation of the spectral-element dynamical core in dry-mass vertical coordinates with
916 comprehensive treatment of condensates and energy, *J. Adv. Model. Earth Syst.*, doi:
917 10.1029/2017MS001257.
- 918 Lin, S.-J. (2004), A 'vertically Lagrangian' finite-volume dynamical core for global mod-
919 els, *Mon. Wea. Rev.*, 132, 2293–2307.
- 920 Medeiros, B., D. L. Williamson, and J. G. Olson (2016), Reference aquaplanet climate in
921 the community atmosphere model, version 5, *J. Adv. Model. Earth Syst.*, 8(1), 406–424,
922 doi:10.1002/2015MS000593.

- 923 Nair, R., H.-W. Choi, and H. Tufo (2009), Computational aspects of a scalable high-order
924 discontinuous galerkin atmospheric dynamical core, *Computers & Fluids*, 38(2), 309 –
925 319, doi:<http://dx.doi.org/10.1016/j.compfluid.2008.04.006>.
- 926 Nair, R. D., and P. H. Lauritzen (2010), A class of deformational flow test cases for linear
927 transport problems on the sphere, *J. Comput. Phys.*, 229, 8868–8887, doi:[10.1016/j.jcp.2010.08.014](https://doi.org/10.1016/j.jcp.2010.08.014).
- 929 Neale, R. B., and B. J. Hoskins (2000), A standard test for agcms including their physical
930 parametrizations: I: the proposal, *Atmos. Sci. Lett.*, 1(2), 101–107, doi:[10.1006/asle.2000.0022](https://doi.org/10.1006/asle.2000.0022).
- 932 Neale, R. B., C.-C. Chen, A. Gettelman, P. H. Lauritzen, S. Park, D. L. Williamson, A. J.
933 Conley, R. Garcia, D. Kinnison, J.-F. Lamarque, D. Marsh, M. Mills, A. K. Smith,
934 S. Tilmes, F. Vitt, P. Cameron-Smith, W. D. Collins, M. J. Iacono, R. C. Easter, S. J.
935 Ghan, X. Liu, P. J. Rasch, and M. A. Taylor (2012), Description of the NCAR Commu-
936 nity Atmosphere Model (CAM 5.0), *NCAR Technical Note NCAR/TN-486+STR*, National
937 Center of Atmospheric Research.
- 938 Pauluis, O., and S. Garner (2006), Sensitivity of radiative–convective equilibrium simula-
939 tions to horizontal resolution, *J. Atmos. Sci.*, 63(7), 1910–1923.
- 940 Randall, D., M. Khairoutdinov, A. Arakawa, and W. Grabowski (2003), Breaking the
941 cloud parameterization deadlock, *Bulletin of the American Meteorological Society*,
942 84(11), 1547–1564.
- 943 Shutts, G. (2005), A kinetic energy backscatter algorithm for use in ensemble prediction
944 systems, *Quart. J. Roy. Meteorol. Soc.*, 131, 3079–3102.
- 945 Skamarock, W. (2011), Kinetic energy spectra and model filters, in: P.H. Lauritzen, R.D.
946 Nair, C. Jablonowski, M. Taylor (Eds.), Numerical techniques for global atmospheric
947 models, *Lecture Notes in Computational Science and Engineering*, Springer, 80.
- 948 Taylor, M., J. Edwards, and A. St-Cyr (2008), Petascale atmospheric models for the com-
949 munity climate system model: new developments and evaluation of scalable dynamical
950 cores, *J. Phys.: Conf. Ser.*, 125, doi:[10.1088/1742-6596/125/1/012023](https://doi.org/10.1088/1742-6596/125/1/012023).
- 951 Wan, H., P. J. Rasch, M. A. Taylor, and C. Jablonowski (2015), Short-term time step con-
952 vergence in a climate model, *Journal of advances in modeling earth systems*, 7(1), 215–
953 225, doi:[10.1002/2014MS000368](https://doi.org/10.1002/2014MS000368).
- 954 Wedi, N. P. (2014), Increasing horizontal resolution in numerical weather prediction and
955 climate simulations: illusion or panacea?, *Philosophical Transactions of the Royal So-*

- ciety of London A: *Mathematical, Physical and Engineering Sciences*, 372(2018), doi:
10.1098/rsta.2013.0289.
- Weisman, M. L., W. C. Skamarock, and J. B. Klemp (1997), The resolution dependence
of explicitly modeled convective systems, *Monthly Weather Review*, 125(4), 527–548,
doi:10.1175/1520-0493(1997)125<0527:TRDOEM>2.0.CO;2.
- Williamson, D. L. (1999), Convergence of atmospheric simulations with increasing
horizontal resolution and fixed forcing scales, *Tellus A*, 51, 663–673, doi:10.1034/j.
1600-0870.1999.00009.x.
- Williamson, D. L. (2013), The effect of time steps and time-scales on parametrization
suites, *Quart. J. Roy. Meteor. Soc.*, 139(671), 548–560, doi:10.1002/qj.1992.
- Williamson, D. L., and J. G. Olson (2003), Dependence of aqua-planet simulations on
time step, *Q. J. R. Meteorol. Soc.*, 129(591), 2049–2064.
- Zhang, G., and N. McFarlane (1995), Sensitivity of climate simulations to the parameter-
ization of cumulus convection in the canadian climate center general-circulation model,
ATMOSPHERE-OCEAN, 33(3), 407–446.